Cell Reports
Medicine

Article

Pan-cancer analysis of spatial transcriptomics reveals heterogeneous tumor spatial microenvironment

Graphical abstract

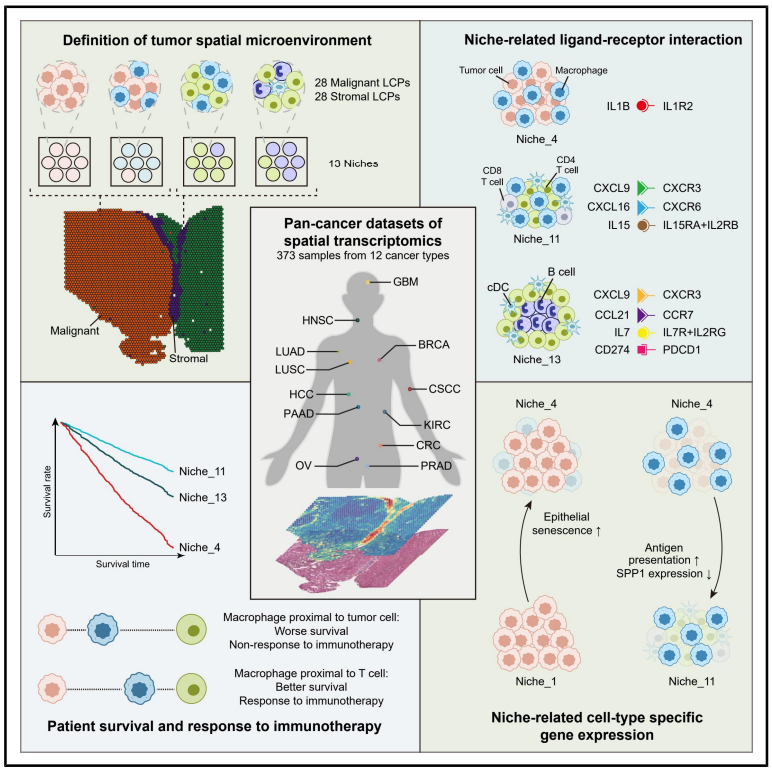

Highlights

- Pan-cancer spatial analysis identifies 56 cellular programs and 13 recurrent niches
- Niche-related LR interaction and cell-type-specific gene expression
- Distinct macrophage niches predict patient prognosis and immunotherapy response

Authors

Jiarong Li, Ping Lin, Heqi Wang, ..., Jiao Yuan, Wanhong Chen, Hong Li

Correspondence

lihong01@sinh.ac.cn

In brief

Li et al. perform a large-scale pan-cancer spatial transcriptomic analysis across 12 cancer types to dissect the tumor spatial microenvironment by identifying LCPs and niches and dissecting related molecular features. These spatially heterogeneous niches are related to patient prognosis and response to immunotherapy.

Li et al., 2026, Cell Reports Medicine 7, 102751
May 19, 2026
https://doi.org/10.1016/j.xcrm.2026.102751

CellPress

Please cite this article in press as: Li et al., Pan-cancer analysis of spatial transcriptomics reveals heterogeneous tumor spatial microenvironment, Cell Reports Medicine (2026), https://doi.org/10.1016/j.xcrm.2026.102751

Cell Reports Medicine

CellPress
OPEN ACCESS

Article

Pan-cancer analysis of spatial transcriptomics reveals heterogeneous tumor spatial microenvironment

Jiarong Li,[1,2] Ping Lin,[1,2] Heqi Wang,[1,2] Zhixuan Tang,[1] Xi Yan,[1,2] Xufeng Chen,[1,2] Jiao Yuan,[1,2] Wanhong Chen,[1,2] and Hong Li[1,2,3,*]

[1]Shanghai Institute of Nutrition and Health, University of Chinese Academy of Sciences, Chinese Academy of Sciences, Shanghai, China
[2]University of Chinese Academy of Sciences, Beijing, China
[3]Lead contact
*Correspondence: lihong01@sinh.ac.cn
https://doi.org/10.1016/j.xcrm.2026.102751

SUMMARY

Tumors are complex systems comprising diverse cell types that form the tumor spatial microenvironment (TSME). We present a pan-cancer spatial transcriptomic analysis of 373 samples across 12 cancer types and identify 56 local cellular programs (LCPs) and 13 recurrent niches. Ligand-receptor analysis reveals niche-shared and niche-specific interactions that drive spatial organization. Notably, gene expression in tumor cells and macrophages depends heavily on their specific location. Furthermore, niches associate significantly with clinical outcomes: macrophages colocalized with tumor cells (Niche_4) correlate with poor prognosis and immunotherapy resistance, while those colocalized with immune cells (Niche_11) predict better survival and treatment response. This systematic dissection of the TSME provides deeper insights into cellular communication and the structural influences governing complex tumor ecosystems.

INTRODUCTION

Tumor is a complex ecosystem composed of tumor cells, as well as other stromal cells and immune cells. Together, they constitute the tumor microenvironment (TME). The TME exerts its biological function in tumor progression, invasion, metastases, and pro-tumor/anti-tumor inflammation.[1] Traditional single-cell RNA sequencing (scRNA-seq) analyses provide a panorama of the cells in the tumor, especially the TME cells. In particular, a series of the pan-cancer scRNA-seq analyses systematically dissects TME cells that are common among tumor types.[2–4] Another algorithm, EcoTyper, uses RNA sequencing (RNA-seq) to define the multicellular communities on the inferred cell type composition.[5,6] Unfortunately, the lack of spatial information makes it difficult to precisely clarify the communications between cells and how these communications take pro-tumor or anti-tumor effects. With the rapid development of the spatial transcriptomics (ST),[7,8] researchers could catch a glimpse of tumor microenvironment spatially.

Recent publications have highlighted the importance of the tumor spatial microenvironment (TSME), which is related to patient outcome and response to treatment.[9] One of the well-known TSMEs is the tertiary lymphoid-like structure (TLS). By applying spatial transcriptomics, the researchers are able to dissect the molecular features of TLS and show that TLS is related to better survival and response to immunotherapy.[10–12] Subpopulations of certain cell type are found in distinct spatial locations.[13–18] For example, *FOLR2*+ macrophages were colocalized with plasma cells, while *NLRP3*+ macrophages were colocalized with neutrophils in colorectal cancer and breast cancer.[13] Furthermore, a recent pan-cancer study has revealed that fibroblasts could be divided into four conserved spatial subtypes based on their neighboring cell types, resulting in different prognostic effects.[16]

Most of these studies have been hampered by the constrained sample sizes and thus have only investigated a single cancer type or a specific cell type. With the accumulation of spatial omics data, it is necessary to more comprehensively characterize TSME across multiple cancer types. Although data of spatial transcriptomics are accumulating,[19,20] in-depth analyses are still needed, especially that related to TSME.

To comprehensively capture and investigate the spatial landscape across tumor types, we conducted a pan-cancer study on the TSME using spatial transcriptomics data. Public data from the 10× Visium platform, one of the most popular technologies for detecting gene expression spatially, were used for analyses. First, we systematically delineated the TSME patterns at different spatial extents across 12 cancer types. Furthermore, we investigated the ligand-receptor (LR) interactions and expression differences under diverse TSMEs. Finally, we adopted external bulk RNA-seq and multiplexed protein imaging data to explore the clinical implications of the TSME (Figure 1A).

Please cite this article in press as: Li et al., Pan-cancer analysis of spatial transcriptomics reveals heterogeneous tumor spatial microenvironment, Cell Reports Medicine (2026), https://doi.org/10.1016/j.xcrm.2026.102751

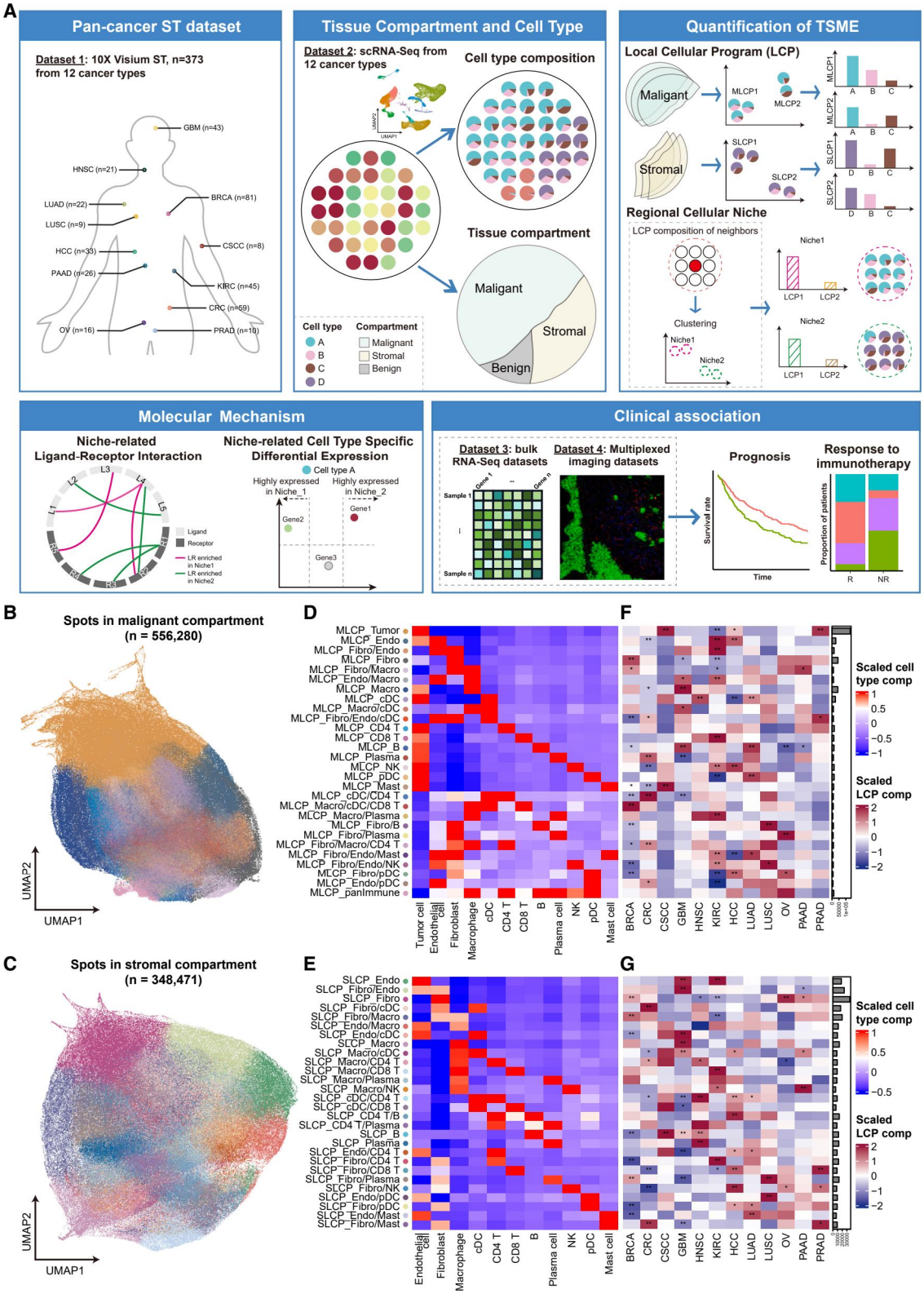

(legend on next page)

Please cite this article in press as: Li et al., Pan-cancer analysis of spatial transcriptomics reveals heterogeneous tumor spatial microenvironment, Cell Reports Medicine (2026), https://doi.org/10.1016/j.xcrm.2026.102751

RESULTS

Overview of the pan-cancer spatial transcriptomics data analysis

To elucidate the TSME heterogeneity of different cancer types, we developed a pipeline to analyze pan-cancer spatial transcriptomics data from the 10× Visium platform (Figure 1A). After quality control of both samples and spots, we generated a pan-cancer spatial transcriptomics atlas of 373 samples containing 993,380 spots from 12 cancer types (Figures S1A–S1C; Table S1), including breast cancer (BRCA), colorectal cancer (CRC), cutaneous squamous cell carcinoma (CSCC), glioblastoma (GBM), head and neck squamous cell carcinoma (HNSC), kidney renal cell carcinoma (KIRC), hepatocellular carcinoma (HCC), lung adenocarcinoma, lung squamous cell carcinoma (LUSC), ovarian cancer (OV), pancreatic adenocarcinoma (PAAD), and prostate adenocarcinoma (PRAD)[11,21–61] (Figure 1A). We next estimated the cell type composition of each spot via RCTD[62] and then classified tissues into Benign, Stromal, and Malignant compartments based on both cell type composition and CNV (copy number variation) profiles (Figures S1D and S2; STAR Methods). Our results show high consistence with well-known histopathology. For example, the ST slides of PAAD exhibit high fractions of Stromal compartment (Figure S1E). The Malignant compartments are dominated by tumor cells. Stromal compartments are dominated by non-parenchymal cells especially fibroblasts (Figure S1F) and could distribute fully in the tumor lesion or at the benign-malignant boundary. We observed the heterogeneous cell type compositions in the spots within the samples (Figures S1G–S1I). After that, the local cellular programs (LCPs) and niches were defined to characterize TSME. To further explore the intrinsic mechanism of these niches, we analyzed the LR interactions and the cell-type-specific gene expression. Finally, we tried to uncover the clinical implications of the TSME using the bulk RNA-seq and multiplexed protein imaging data, to reveal its association with patient prognosis and response to immunotherapy.

Characterization of the heterogeneity of local cellular programs

Considering the large difference in the cell type composition between Malignant and Stromal compartments (Figure S1D), LCPs were identified by the unsupervised clustering of the cell type composition of the spots in Malignant and Stromal compartments, called MLCP (Malignant LCP) and SLCP (Stromal LCP), respectively (Figures 1B and 1C; STAR Methods). Consequently, we obtained 28 MLCPs and 28 SLCPs, named by the most abundant cell types (Figures 1D, 1E, S3A, and S3B; Table S4). The contents of these LCPs show high variation across tumor types (Figures 1F–1G). For example, MLCP_Tumor emerges as the predominant MLCP, which shares higher fraction in CSCC, HCC, and PRAD and less abundance in KIRC (Figure 1F). Similarly, SLCP_Fibro accounts for the largest number among all SLCPs, which is higher in BRCA, OV, and PAAD (Figure 1G; Table S4).

Next, we sought to resolve the spatial distribution of LCPs. We developed a pipeline to dissect the spatial distribution of LCP from two facets (Figure S3E). First, we scrutinized the assortativity of LCPs, that is, the degree of LCP self-aggregation. MLCP_Tumor has the highest self-connectivity across samples among the MLCPs, reflecting the local congregation of tumor cells (Figure S3F). MLCP_Fibro/Plasma, MLCP_Plasma, MLCP_Macro, MLCP_Fibro, and MLCP_Macro/Plasma are also highly self-connected (Figure S3F). For SLCPs, surprisingly, SLCP_CD4 T/B has the highest self-connectivity among SLCPs, although it ranks seventh in terms of SLCP quantity, indicating a highly organized structure composed of CD4 T and B cells (Figures 1G and S3F). Then we detected spatial adjacent communities, which reflect the colocalization among multiple niches. Totally, we identified 10 communities. Among them, there is a community containing LCPs related to plasma cells, indicating the TSME with plasma cells aggregation. Besides, there are two macrophage-related communities, one consisting of MLCP_Fibro/Macro, MLCP_Endo/Macro, SLCP_Macro, SLCP_Fibro/Macro, and SLCP_Endo/Macro and the other one consisting of MLCP_Macro/cDC, MLCP_Macro/cDC/CD8 T, SLCP_Macro/cDC, SLCP_Macro/CD8 T, SLCP_cDC/CD8 T, and SLCP_Macro/NK (Figure S3G). It implied that macrophages would have different TSME patterns.

Consensus spatial niches in pan-cancer samples

Given that the locations of the LCPs arrange into distinct spatial organizations, we then considered the neighborhood of spots to define the TSME over a larger spatial extent, which is called niche here (Figure 1A). Thirteen consensus niches were identified among 12 cancer types (Figures 2A, 2B, and S4A; Table S5; STAR Methods). Niche_1–Niche_6 primarily consist of MLCPs. Niche_1 is mostly composed of MLCP_Tumor, and we deduce that this niche represents the aggregation of tumor cells and the lack of infiltration of other TME cells. Niche_2 is mainly composed of MLCP_Endo and MLCP_Fibro/Endo, which inflect the TME of the tumor cells colocalized with endothelial cells. Niche_3 consists of MLCP_Fibro, which depicts the TME of fibroblasts colocalized with tumor cells. Niche_4 is associated with MLCP_Macro, in which macrophages and tumor cells are located in the same area. Spots of Niche_5 and Niche_6 are MLCPs with lymphocytes, which signify the TME of immune cell infiltration in the tumor. Niche_7–Niche_13 consist mainly of SLCPs. Niche_7 is composed mainly of SLCP_Endo and SLCP_Fibro/Endo, which may represent vessels in the Stromal compartment. The spots of Niche_8 are mostly SLCP_Fibro, which is dominated by fibroblasts. Spots in Niche_9 coexist

Figure 1. Overview of the study and local cellular programs across pan-cancer samples

(A) Overview and workflow of the study.

(B and C) Uniform manifold approximation and projection plot of spots in the Malignant (B) and Stromal (C) compartments embedding by their cell type compositions. The points represent spots and are colored by the labels of MLCPs and SLCPs.

(D and E) Scaled mean composition of the cell types in MLCPs (D) and SLCPs (E).

(F and G) Scaled composition of MLCPs (F) and SLCPs (G) in different tumor types, and the total number of spots in each LCP. *$p < 0.01$ and **$p < 0.001$ represent the fraction of LCPs that is significantly higher or lower in specific tumor type compared to the others, tested with Wilcox rank-sum test.

Please cite this article in press as: Li et al., Pan-cancer analysis of spatial transcriptomics reveals heterogeneous tumor spatial microenvironment, Cell Reports Medicine (2026), https://doi.org/10.1016/j.xcrm.2026.102751

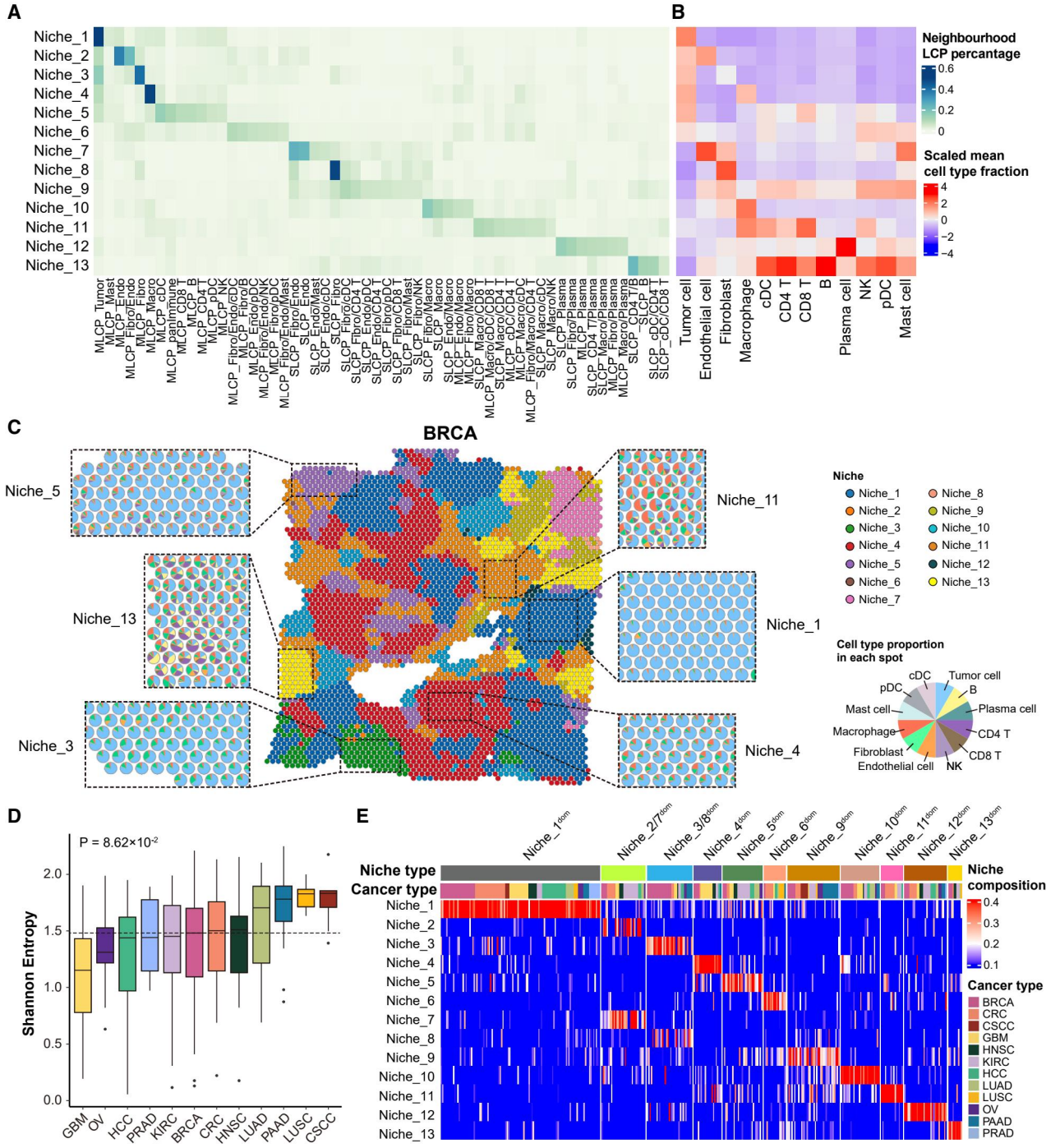

Figure 2. Consensus niches in pan-cancer and intra-/inter-tumor heterogeneity

(A) Mean LCP composition of the neighboring spots in different niches.

(B) Mean cell type composition of the spots in different niches.

(C) *In situ* presentation of the niches and cell type fraction of the spots in an example sample. The spatial pattern of the niches is shown in the middle, and the cell type composition of the spots in typical regions is shown with pie plots.

(D) Bar plot showing the Shannon entropy calculated from the niche composition of each sample, stratified by cancer types. *p* values were calculated by ANOVA across tumor types.

(E) Heatmap displays the niche composition of the samples, and the tracks on the top of the heatmap show niche types and cancer types of the samples.

Please cite this article in press as: Li et al., Pan-cancer analysis of spatial transcriptomics reveals heterogeneous tumor spatial microenvironment, Cell Reports Medicine (2026), https://doi.org/10.1016/j.xcrm.2026.102751

with mesenchymal cells and immune cells. Niche_10 is predominantly characterized by SLCPs where macrophages coexist with stromal cells. Niche_11 is the niche with SLCPs that colocalize with macrophages and other immune cells. Niche_12 is composed mainly of MLCPs and SLCPs containing plasma cells. The spots of Niche_13 are mainly SLCP_B, SLCP_cDC/CD4 T, and SLCP_cDC/CD8 T, indicating an immune TSME that aggregates B cell, cDC (conventional dendritic cell), CD4 T, and CD8 T, which appears to be a TLS-like niche (Figures 2A, 2B, and S4A; Table S5).

Interestingly, plasma cells and B cell were distributed in Niche_12 and Niche_13, respectively. We found a higher proportion of cDC, CD4 T, and B cell in Niche_13 but a higher proportion of plasma cell in Niche_12 (Figure S5A). Also, plasma cell-related genes, such as *MZB1*, have higher expression in Niche_12, while B cell-related genes, such as *MS4A1* have higher expression in Niche_13 (Figures S5A, S5C, and S5D). Moreover, the genes of antibodies are also differently expressed in two niches. Most of the antibody genes, such as *IGHG1*, *IGKC*, *IGHA1*, and *JCHAIN*, are highly expressed in Niche_12, while *IGHD* is highly expressed in Niche_13 (Figures S5B, S5C, and S5E), suggesting the plasma cells in Niche_12 have undergone antibody class switch but B cells in Niche_13 have not. These results indicate B cell and plasma cell are located in different spatial microenvironment, and execute different biological functions. In a recent study on GBM, patients of B:T-TLS and PC-TLS were distinguished, consistent with our results that B cells and plasma cells are in different niches.[63]

We further validated our defined niches using public high-resolution spatial transcriptomics datasets from Vizgen MERSCOPE.[62] The cell type colocalization patterns seen in 10× Visium could also be observed in subcellular-resolved technologies (Figures S6A–S6G; STAR Methods). For example, we found the B cell-mediated and plasma-cell-mediated niches, as well as the colocalization of macrophages and epithelial cells and the colocalization of macrophages with the immune cells (Figure S6H).

Intra- and inter-tumor heterogeneity of spatial niches

Generally, more than one niche could be found in each sample, reflecting intra-tumor TSME diversity (Figures 2C, S4B, and S4C). Quantitative measurement of intra-tumor TSME heterogeneity revealed that CSCC, LUSC, and PAAD have more extensive diversity than the other tumor types (Figure 2D). For the inter-tumor diversity, samples were grouped into 11 clusters on the basis of their similarity in niche composition and named based on their dominant niches (Figure 2E). Although each cluster encompassed multiple cancer types, individual tumor type still exhibited preferences for the specific cluster (Figures 2E and S5F). Niche1^{dom} was enriched in PRAD (80.0%) and HCC (50.0%), which suggests that TME cells are depleted in the majority of the patients with these two tumor types. Niche2/7^{dom} was enriched in KIRC (24.4%), implying that endothelial cell is an important component in part of KIRC patients. Niche3/8^{dom} was enriched in BRCA (22.5%), implying that fibroblast is an important component in part of BRCA patients (Figures 2E and S5F). The remaining clusters, which are traditionally noted as "Immune-hot" tumors, could also be heterogeneous due to their diverse immune cell types and spatial distributions. For example, Niche4^{dom} was enriched in GBM (21.9%), while Niche9^{dom} was enriched in CSCC (62.5%) and PAAD (42.3%) (Figures 2E and S5F). Yet, multiple niche types were still observed in the same cancer type (Figure S5F). Among our collected pan-cancer datasets, one CRC cohort provides the labels of microsatellite unstable (MSI-H) and microsatellite stable (MSS) subtypes.[50] Totally, there are 11 MSI-H samples and 14 MSS samples. We found that the niche type composition is different between MSI-H and MSS patients, in which Niche_1^{dom} occupied most of the MSS samples, while the immune-cell-enriched niches were encountered in MSI-H patients (Figure S5G, left). Another two HCC immunotherapy cohorts contain 6 responders and 8 non-responders.[24,32] Also, the niche type composition is different between responders and non-responders. Over half of the non-responders belong to Niche_1^{dom}, and the immune-enriched niches, such as Niche_12^{dom} and Niche_13^{dom}, are enriched in the responders (Figure S5G, right).

To illustrate the validity, we compared the spatial niches defined here with the spatial domains clustered by gene expression (Figures 2C, S4D, and S4E; STAR Methods). Multiple niches dominated by non-parenchymal cells (Niche_7–13) are allocated to one domain, indicating that the expression-based domain may not well represent immune heterogeneity due to the complexity and similarity of different immune cells. Niche_1 and Niche_4 are allocated to multiple different domains; these domains may reflect differences in tumor cell expression among different cancer types, but they are not conducive to identifying consensus TSME across cancers. On the other hand, we also compared the sample clusters with previously defined immune subtypes from pan-cancer bulk RNA-seq[64,65] (Figure S5H; STAR Methods). The relationship between tumor type and The Cancer Genome Atlas (TCGA) immune subtype was consistent with the original study. For example, GBM is enriched in "Lymphocyte depleted" subtype and KIRC was enriched in "Inflammatory" subtype (Figure S5H). The "IFN-γ dominant" subtype could be further classified into several niche types, implying that our defined niche types could better capture the diversity of immune components across patients (Figure S5I). Overall, these results prove that our defined niches based on spatial transcriptomics have better performance in depicting intra- and inter-tumor TSME heterogeneity.

Systematic dissection of ligand-receptor interactions within niches

A niche represents a complex spatial pattern in which adjacent cells are composed of specific cell types. We hypothesized that LR interaction is one of the most pivotal factors driving cell aggregation and the establishment of niches, thus affecting the biological function of the niches. Therefore, we tried to identify the LR pairs that occur within the niches. The LR interaction score for each spot was defined by the coordinated gene expression of ligands and receptors. Niche-related LR pairs were selected by first comparing the LR scores across spots within a sample and then integrating the results from all samples via meta-analysis (Figures 3A and S7A; STAR Methods). The comparison of niches showed that some LRs are present in only one single niche (Figure 3B; Table S6), such as EREG-EGFR + ERBB2 in Niche_1 and PTPRC-CD22 in Niche_13. In

Please cite this article in press as: Li et al., Pan-cancer analysis of spatial transcriptomics reveals heterogeneous tumor spatial microenvironment, Cell Reports Medicine (2026), https://doi.org/10.1016/j.xcrm.2026.102751

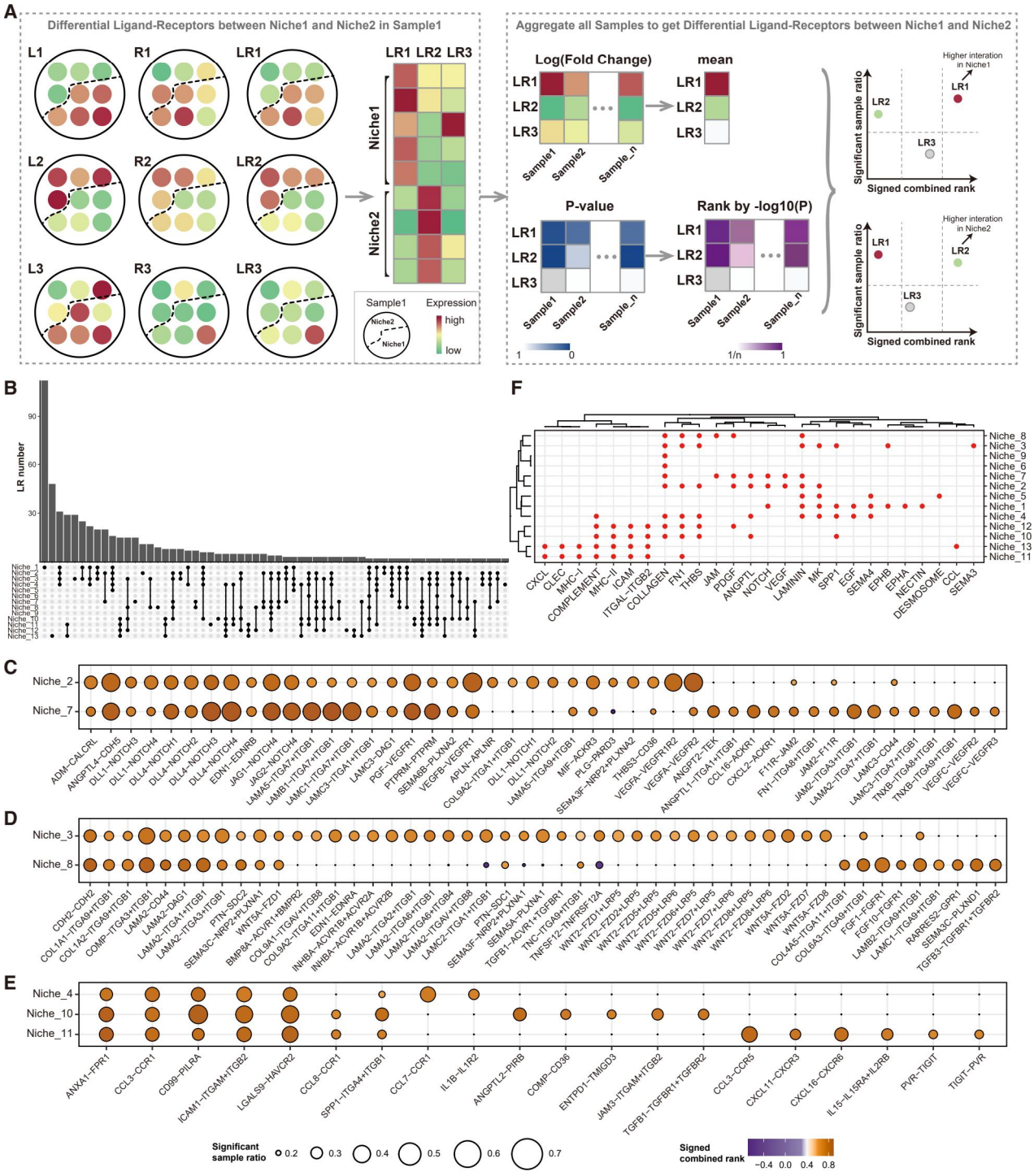

Figure 3. Niche-shared and niche-specific ligand-receptor interactions

(A) A schematic of the identification of niche-related LR interactions.

(B) The number of LR interactions in the niches.

(C–E) Shared and specific LR interactions of endothelial cell-related (C), fibroblast-related (D), and macrophage-related niches (E). The dot color represents the signed combined ranks by the rank-based meta-analysis, and the dot size represents the ratio of samples with significantly higher or lower LR interaction scores under the confidence of 0.95.

(F) Enriched LR interaction pathways of the niches. The red dots indicate that the LR interactions of the niches are enriched in specific pathways with $p < 0.05$ according to Fisher's exact test.

Please cite this article in press as: Li et al., Pan-cancer analysis of spatial transcriptomics reveals heterogeneous tumor spatial microenvironment, Cell Reports Medicine (2026), https://doi.org/10.1016/j.xcrm.2026.102751

contrast, other LRs are found in multiple niches (Figure 3B); for example, Niche_2 and Niche_7 shared 20 common LR interactions.

Niches with the same major cell types not only share many overlapping LR pairs but also exhibit distinct LR pairs due to the difference in colocalized cell types (Figure 3B; Table S6). For example, Niche_2 and Niche_7 predominantly harbor endothelial cells, both of which exhibit VEGFB-VEGFR1 and ANGPTL4-CDH5 interactions, while ANGPT2-TEK and VEGFC-VEGFR2 interactions only occur in Niche_7 and VEGFA-VEGFR1R2 and SEMA3F-NRP2 + PLXNA2 interactions only occur in Niche_2, which probably indicates communication between tumor cells and endothelial cells (Figure 3C; Table S6). Niche_3 and Niche_8 are niches dominated by fibroblasts, where common LR pairs are seen, such as COMP-ITGA3 and LAM2-CD44, while FGF1-FGFR1 and FGF10-FGFR1 only occur in Niche_8 and INHBA-ACVR1B + ACVR2A and SEMA5A-PLXNA1 only occur in Niche_3, which may be the communications between tumor cells and fibroblasts (Figure 3D; Table S6). Similarly, Niche_4, Niche_10, and Niche_11 are niches containing macrophages; there are common and shared LR interactions reflecting the communication between macrophages and other cell types (Figure 3E; Table S6).

We then dissected the LR interactions at the pathway level and observed niche-specific and shared pathways (Figure 3F; Table S7; STAR Methods). For example, the EPHA ($p = 4.01 \times 10^{-7}$) and NECTIN ($p = 1.39 \times 10^{-2}$) pathways were enriched only in Niche_1, and this enrichment might represent the communication mechanism between tumor cells. Among them, nectin family proteins are involved in cell adhesion and proliferation, which is related to poor prognosis in many types of cancer.[66,67] COMPLEMENT, MHC-II, ICAM, and ITGAL-ITGB2 are enriched in multiple immune-related niches (Niche_10, Niche_11, Niche_12, and Niche_13) (Figure 3F; Table S7), indicating that these LR interaction pathways are common features of immune cell-related niches. Even for the shared pathway, the LRs used by different niches may vary. Taking the NOTCH pathway as an example, it is enriched in Niche_1 ($p = 0.0119$), Niche_2 ($p = 3.25 \times 10^{-11}$), and Niche_7 ($p = 1.89 \times 10^{-8}$) (Figure 3F; Table S7); however, *DLL3*-mediated LR interactions are only present in Niche_1, whereas *DLL1*- and *DLL4*-mediated LR interactions are present in Niche_2 and Niche_7, suggesting their roles in angiogenesis (Figure S7B; Table S6). Similar phenomena could also be found in other pathways, such as COLLAGEN and LAMININ signaling pathways (Figures S7C and S7D; Table S6). Taken together, our analyses revealed that LR signaling may be involved in the formation and biological function of diverse niches in pan-cancer microenvironments.

Immune-related LR interactions take action in immunomodulation

Next, we investigated genes that play crucial roles in immune cell recruitment and immune regulation. First, we examined the interaction between chemokines and their receptors in all the niches (Figures 4A and S8A; Table S6). CXCL12-CXCR4 occurs in Niche_7, Niche_8, Niche_9, Niche_10, Niche_11, Niche_12, and Niche_13 (Figure S8B), which is consistent with its diverse functions in fibrosis,[68] angiogenesis,[69,70] plasma cell migration,[11] and immune microenvironment formation[71,72] reported in previous studies. CCL15-CCR1 occurs only in Niche_1, and CCL7-CCR1 occurs only in Niche_4 (Figure S8C). Chemokine interactions are most active in Niche_11 and Niche_13 (Figure 3F). In both of these niches, CXCL9-CXCR3 (Figure 4B), CCL5-CCR5, CCL5-CCR1, and CXCL10-CXCR3 (Figure S8D) interactions occur, in which *CXCL9* is suggested to promote anti-tumor immunity[73] and response to immunotherapy.[74,75] There are also niche-specific differences, such as CXCL16-CXCR6 (Figure 4B) and CCL3-CCR5 (Figure S8D) in Niche_11 and CCL21-CCR7 (Figure 4B), CCL19-CCR7, and CXCL13-CXCR5 (Figure S8D) in Niche_13. *CCL21*, *CCL19*, and *CXCL13* are commonly seen in TLS.[76,77] These results demonstrate the diversity and complexity of chemokine interaction network in different niches.

The interactions between interleukins (ILs) and their receptors also play central roles in immunity. IL1B-IL1R2 interaction was exclusively found in Niche_4 (Figures 4C, 4D, and S8E). Macrophage-secreted *IL1B* has been proven to contribute to tumor progression.[78–80] The IL7-IL7R + IL2RG interaction was greatest in the TLS-like Niche_13 (Figure 4D). Previous studies have reported the role of *IL7* in the recruitment of lymphoid cells in the formation of TLS.[76,77,81] The IL15-IL15RA + IL2RG interaction is found in Niche_11 (Figure 4D), of which *IL15* is related to the proliferation and activation of T cell and natural killer (NK).[81] Both *IL7* and *IL15* are the members of the IL-2 family with similar bioactivities in activating T cell,[81] but they take effects in different niches.

Then, we collected immune-activated and immune-suppressive LR pairs to investigate the niches in which these interactions occur[82–84] (Table S8). Niche_13 harbors more immune-activated and immune-suppressive LRs than other niches, consistent with its diverse immune cell types (Figures 4E, S8F, and S8G; Table S6). PD-1 (*PDCD1*) and PD-L1 (*CD274*) are the most important immune checkpoints in cancers, and their interaction occurs in Niche_13 (Figures 4E and S8G).

Finally, we delineated the contribution of these immune-related LR pairs to prognosis across 21 tumor types in the TCGA datasets (Figure 4F; STAR Methods). The abovementioned Niche_11- and Niche_13-related LR pairs, such as CXCL9-CXCR3, CXCL11-CXCR3, CCL19-CCR7, CXCL13-CXCR5, CCL19-CCR7, CCL21-CCR7, IL15-IL15RA + IL2RB, IL7-IL7R + IL2RG, and CD274-PDCD1, are associated with better survival in at least seven tumor types (Figures 4F and S8H), while IL1B-IL1R2, which occurs in Niche_4, is associated with worse survival in seven tumor types (Figures 4F and S8I). In summary, we deciphered the LR interactions that are important for TSME remodulation, and these LR interactions are related to the outcomes of patients.

Gene expression of the cell types reliant on their niches located

One cell type may be involved in different niches. To further understand the associations between gene expression in cells and the local microenvironment in the niches, we proposed a strategy to identify niche-related cell type-specific differential expression gene (NCDEG) (Figure 5A; STAR Methods).

First, we analyzed tumor cell-specific NCDEGs in niches dominated by MLCPs (Niche_1, Niche_2, Niche_3, Niche_4, Niche_5 and Niche_6). Niche_1, with nearly pure tumor cells,

Please cite this article in press as: Li et al., Pan-cancer analysis of spatial transcriptomics reveals heterogeneous tumor spatial microenvironment, Cell Reports Medicine (2026), https://doi.org/10.1016/j.xcrm.2026.102751

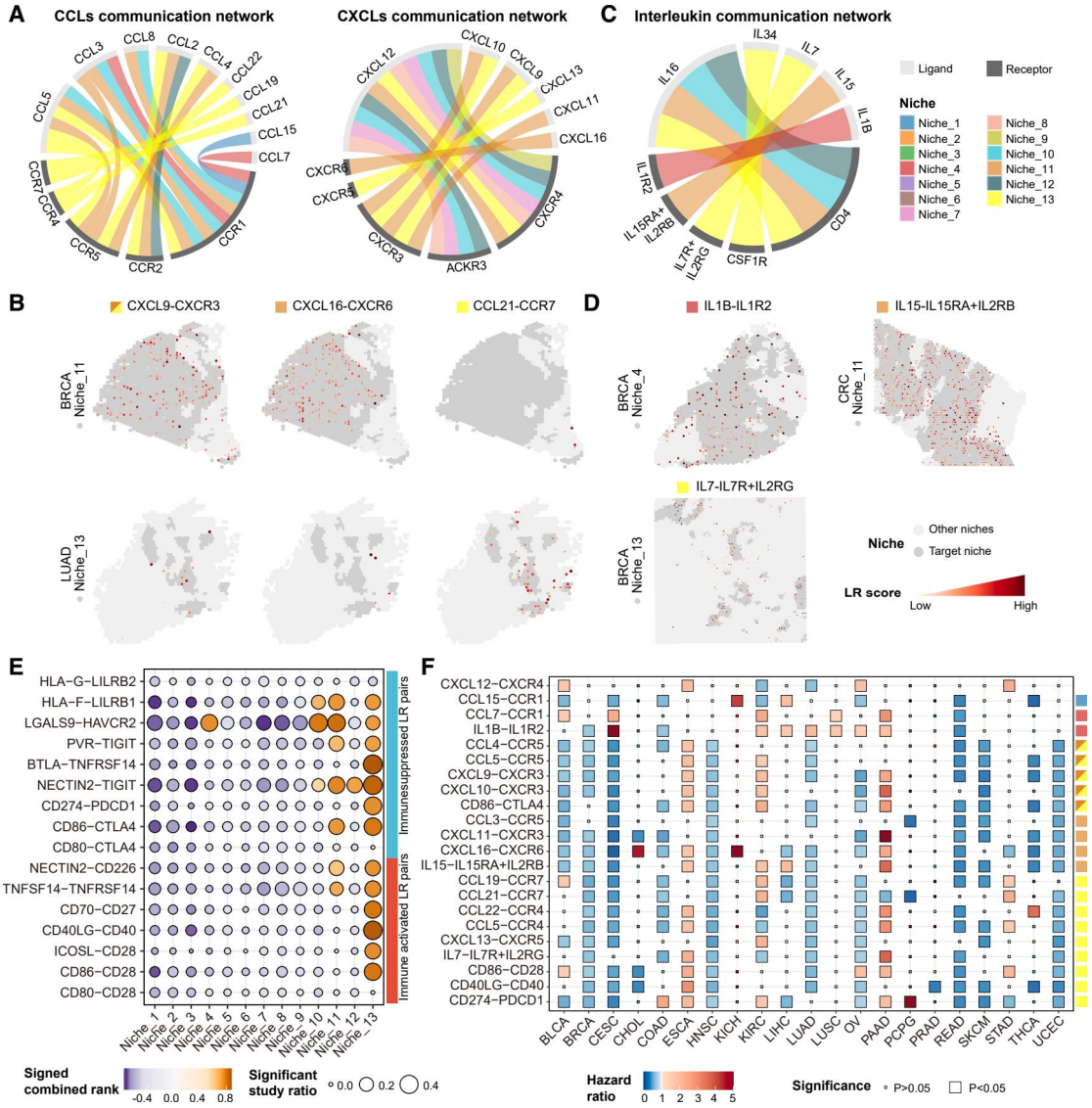

Figure 4. Immune-related LR interactions and their associations with patient survival

(A and C) Chord diagrams showing the niche-related LR interactions of chemokines (A) and interleukins (C). The color of the flows represents which niches the LR interactions occur in.

(B and D) *In situ* display of LR interaction scores of niche-related chemokine (B) and interleukin (D) pairs. The spots colored in dark gray show the region of specific niche for observation of the LR interaction, while the ones colored in light gray represent the remaining niches. The color and the size of the smaller red dots represent the interaction score of the LRs.

(E) Immune-activated and immune-suppressive LR interactions of different niches. The dots are colored by the signed combined ranks by the meta-analysis, and their sizes represent the ratios of samples with significantly higher or lower LR interaction scores ($p < 0.05$).

(F) Survival analysis of the LR pairs by TCGA datasets. In the heatmap, the block color represents the hazard ratio (HR) and the block size represents the p value. The annotation block on the right represents which niche the LR interactions occur in, whose color is the same as that of Figure 4A.

was used as a reference to elucidate differentially expressed genes of tumor cells in each other niches (Figure S9A; Table S9). Subsequently, enrichment analysis was conducted for previously reported tumor cell states[26,85] (Figure 5B; Table S10). NCDEGs that are more highly expressed in tumor cells in Niche_5 and Niche_6 are associated with allograft rejection (adjusted $p = 7.94 \times 10^{-5}$ and 1.34×10^{-2}) and interferon-gamma response (adjusted $p = 5.50 \times 10^{-18}$ and 6.85×10^{-6}) (Figure 5B; Table S10), such as *CFB* (Figure 5C). These immune-related transcriptional programs may inhibit tumor progression.[86] The highly expressed genes of tumor cells in Niche_3 and Niche_4 are enriched in epithelial-mesenchymal transition (EMT) programs (Figure 5B; Table S10), which suggests that the tumor cells that colocalized with fibroblasts or macrophages have greater potential to undergo EMT, which is one of the causes of tumor metastases. A representative EMT-related

Please cite this article in press as: Li et al., Pan-cancer analysis of spatial transcriptomics reveals heterogeneous tumor spatial microenvironment, Cell Reports Medicine (2026), https://doi.org/10.1016/j.xcrm.2026.102751

CellPress
OPEN ACCESS

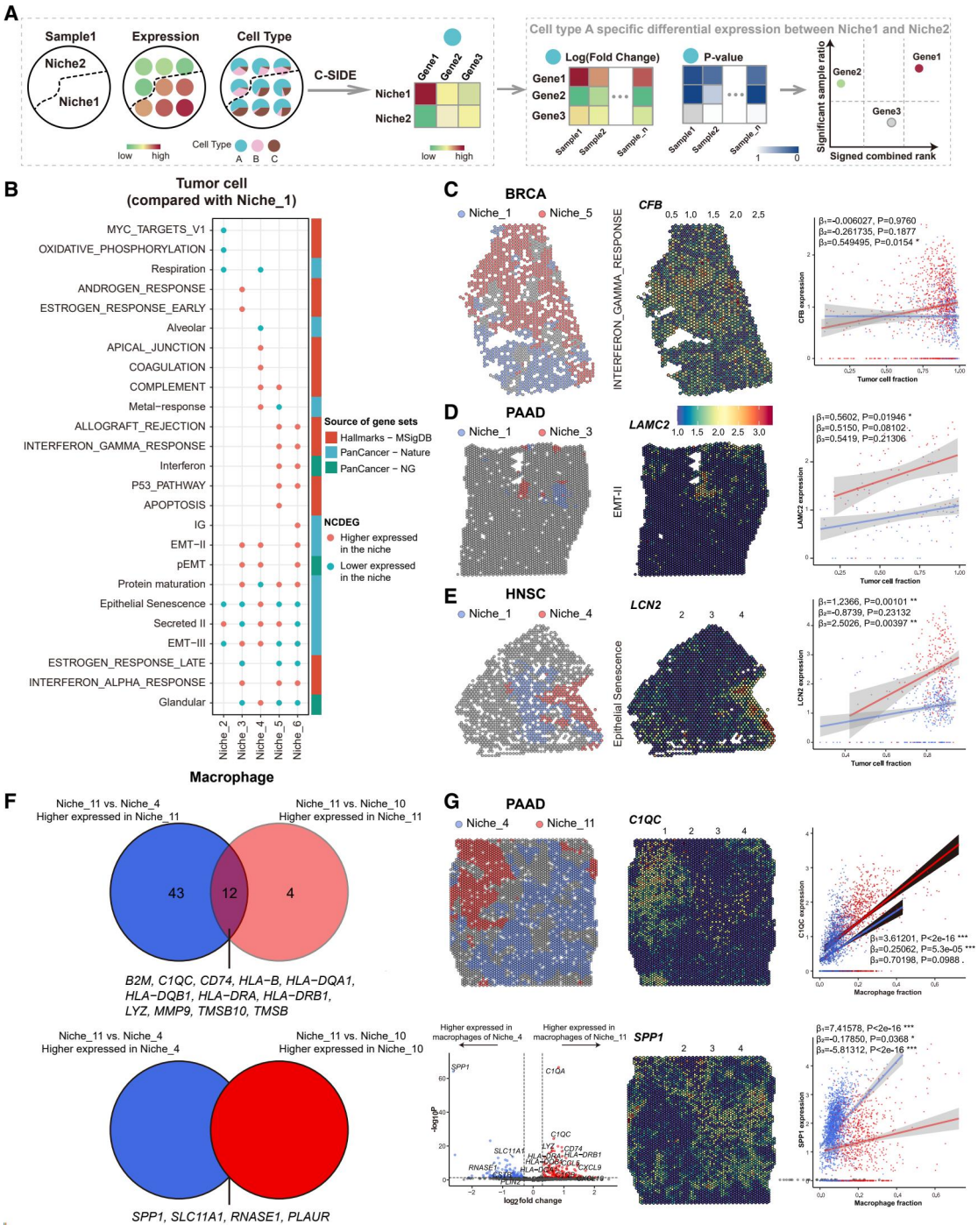

Figure 5. Niche-related cell type-specific differential expression gene

(A) Schematic of the identification of NCDEGs.

(B) Enriched pathways of tumor cell-specific NCDEGs in Niche_2–Niche_6, compared to Niche_1. The red and cyan dots represent the NCDEGs, enriched in specific pathway, selected with $p < 0.05$ by Fisher's exact test.

(C–E) Representative samples showing higher expression genes in the niches: *CFB* in Niche_5 (C), *LAMC2* in Niche_3 (D), and *LCN2* in Niche_4 (E). (Left) The spatial location of the niches. (Middle) The *in situ* expression of the genes. (Right) The scatterplot illustrating the relationships among gene expression, tumor cell fraction, and niches, in which the regression models quantitatively measure the relationship among these three variables.

(legend continued on next page)

gene in Niche_3 is *LAMC2* (Figures 5D and S9A), which has been proven to be related to fibroblast infiltration.[87,88] In addition, we observed that tumor cells in Niche_4 presented higher expression of genes related to epithelial senescence (adjusted $p = 4.89 \times 10^{-5}$, Figure 5B; Table S10), such as *LCN2* (Figures 5E and S9A). Senescent cells have been shown to secrete factors that attract macrophages,[89,90] and *LCN2* expression in tumor cells is related to macrophage in leptomeningeal metastasis,[91] which partly explains the observed macrophage and tumor co-localization in Niche_4.

Macrophages participate in multiple niches. We then investigated the differential expression of macrophages colocalized with other immune cells in Niche_11, compared with those colocalized with tumor cells in Niche_4 or stromal cells in Niche_10 (Figure S9B; Table S11). To determine whether these spatially related NCDEGs are associated with macrophage cell states, the NCDEGs were mapped to a recently published study of pan-cancer macrophage subtypes.[92] We found that NCDEGs highly expressed in Niche_11 are related to the 2_C3Mac and 8_IFNGMac subtypes, whereas NCDEGs highly expressed in Niche_4 or Niche_10 are related to the 6_SPP1AREGMac and 3_ICMac subtypes (Figure S9B). M1/M2 polarization is a widely recognized theory used to explain the biological function of macrophages. NCDEGs highly expressed in macrophages of Niche_11 are related to M1 polarization, whereas those highly expressed in Niche_4 or Niche_10 are related to M2 polarization (Figure S9B). We are particularly interested in Niche_11-specific genes since they may mediate the microenvironment between macrophages and other immune cells. The intersection of the NCDEGs shows 12 genes had higher expression in macrophages in Niche_11 (Figure 5F), including *LYZ*, *C1QC*, and multiple genes related to antigen presentation (*HLA-DQA1*, *HLA-DQB1*, *B2M*, and *CD74*), implying active immune-related functions, particularly in antigen presentation. On the other hand, 4 genes (*SPP1*, *RNASE1*, *PLAUR*, and *SLC11A1*) had lower expression in macrophages in Niche_11 (Figures 5G and S9C). Among them, *SPP1* is a well-known marker of a macrophage subtype, related to worse prognosis.[46,93] Overall, we successfully identified genes that were differentially expressed in typical cell types among different niches.

Niche is related to patient survival and treatment response

To investigate the clinical implications of the niches, we incorporated bulk RNA-seq data by assigning the most likely niche label to each bulk sample based on the deconvoluted cell type composition (Figures S10A–S10C; STAR Methods). We found that the niche types are differentially distributed across the molecular subtypes of CRC,[94] HNSC,[95] LIHC (liver hepatocellular carcinoma),[96] and KIRC.[97] For example, we observed higher fraction of Niche_1-like patients in iCluster:2 and iCluster:3 HCC subtypes, while the patients of iCluster:1 were composed of more other niche types (Figure S10D). The prognostic analysis of 5,162 patients from 11 cancer types revealed distinct survival times among niches[98] (Figure 6A; Table S1; STAR Methods). Patients of Niche_11-like, Niche_12-like, and Niche_13-like have longer overall survival (OS), whereas patients of Niche_9-like, Niche_10-like, and Niche_4-like have worse survival (Figure 6A). In particular, among macrophage-related niches, patients of Niche_11-like had longer OS than those of Niche_4-like and Niche_10-like (Figures 6A and S10E).

We also collected bulk RNA-seq data from 776 patients from eight immunotherapy cohorts prior to treatment.[12,99–105] The similar strategy described above for assigning niche types was used (Figure S10F; Table S1). The meta-analysis of eight cohorts revealed that patients of Niche_13-like ($p = 0.086630$) had a better response to immunotherapy, whereas those of Niche_4-like ($p = 0.008260$) are related to non-response to immunotherapy (Figure 6B; STAR Methods). These two niches were also analyzed in each cohort. Although there were differences in the odds ratios among the cohorts, they exhibit the same trend (Figures 6C and S10G).

The spatial distribution of macrophages is an important biomarker for patient prognosis and treatment response

Based on the analyses above, we observed that the colocalization of macrophages with different cell types has a significant effect on the characteristics of tumors. The colocalization of macrophages and tumor cells (corresponding to Niche_4) is related to worse prognosis, whereas the colocalization of macrophages and other immune cells, such as T cells and cDC (corresponding to Niche_11), is related to better prognosis. To further validate this phenomenon at the single-cell spatial resolution, we utilized four datasets from the multiplexed protein imaging technologies.[106,107] First, we classified macrophages according to their spatial distances to tumor cells and T cells: M01 macrophages are proximal to T cells and M02 macrophages are proximal to tumor cells (Figure 6D). We then stratified patients into four groups according to the proportion of M01 and M02, including G1 ($M01^{hi}M02^{lo}$), G2 ($M01^{hi}M02^{hi}$), G3 ($M01^{lo}M02^{lo}$), and G4 ($M01^{lo}M02^{hi}$) (Figures 6D and 6E; STAR Methods). The three datasets of non-small cell lung cancer[15] ($p = 0.0034$), HCC[108] ($p = 0.015$), and BRCA[109] ($p = 0.0041$) revealed that patients from the four patient groups had different survival outcomes. Specifically, patients of G1 have better OS, while the patients of G4 have poorer OS (Figure 6F). Another cohort of patients with melanoma before anti-PD-1 therapy was used to validate the response to immunotherapy.[110] The distribution of the four patient groups differed between responders and non-responders, which was marginally significant ($p = 0.074$, Figure 6H). The responders have higher proportion of M01-high patients (G1 and G2, $p = 0.04718$), whereas the proportion of the G4 subgroup showed an increasing trend in non-responders ($p = 0.06522$).

Our findings are consistent with several studies on single cancer. One study on small cell lung cancer reported an MT^{2} niche, reflecting the colocalization of macrophages with CD8 T cells and NK T cells, which is associated with better prognosis and

(F) Comparison of NCDEGs among macrophage-related niches. Venn diagrams show the intersections of NCDEGs of Niche_11 compared to Niche_4 and Niche_10, related to Figure S9B.
(G) A representative sample to show the NCDEGs in Niche_4 and Niche_11. (Top left) Spatial location of the niches is shown. (Bottom left) The volcano plot of the result from C-SIDE. (Middle and right) *In situ* expression patterns and the scatterplots of *C1QC* and *SPP1*.

Please cite this article in press as: Li et al., Pan-cancer analysis of spatial transcriptomics reveals heterogeneous tumor spatial microenvironment, Cell Reports Medicine (2026), https://doi.org/10.1016/j.xcrm.2026.102751

CellPress
OPEN ACCESS

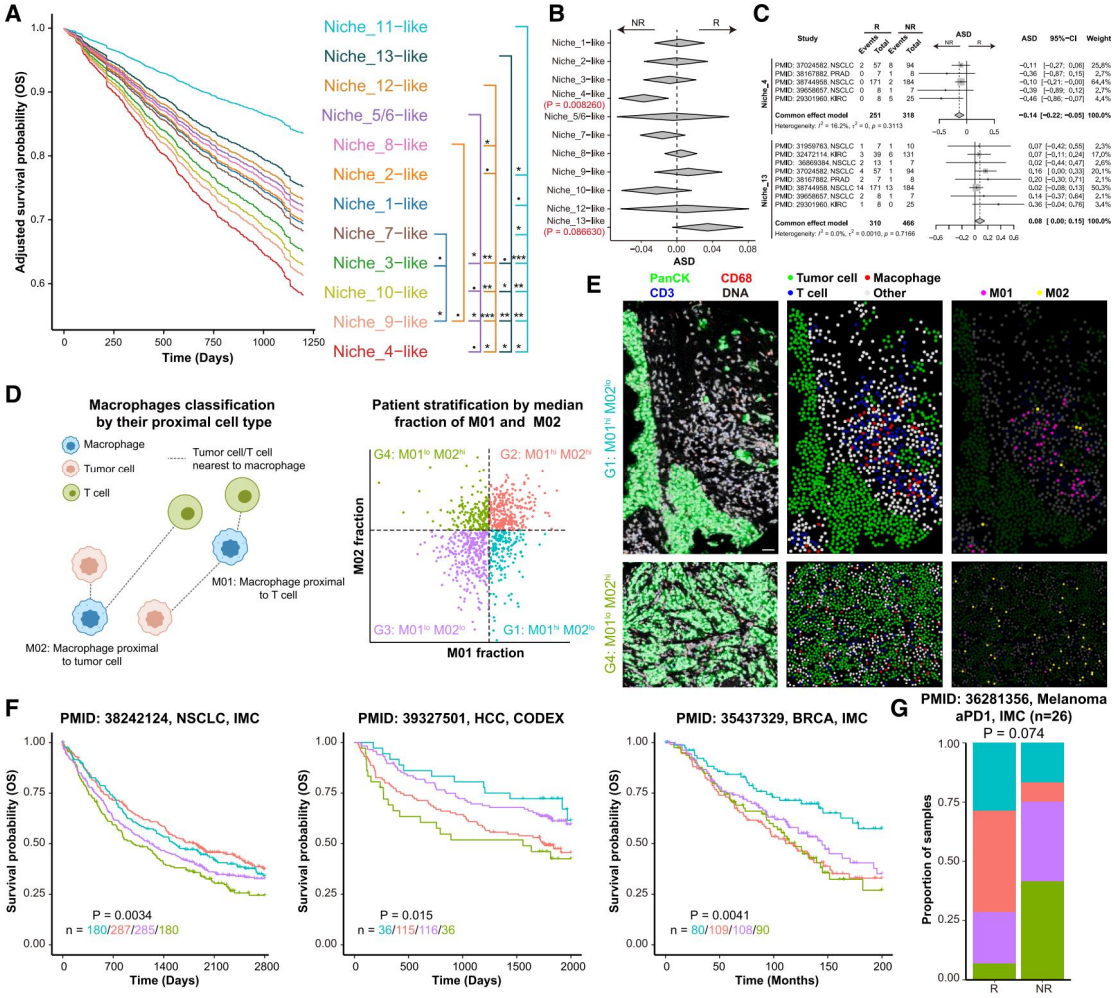

Figure 6. Clinical implications of the niches and spatial distribution of macrophages

(A) The association of the niche types with patient survival. (Left) Simulated survival curves of different niche types adjusted by tumor types based on pan-cancer bulk RNA-seq datasets. The curves are colored by the assigned niche types. (Right) Pairwise comparison of the survival of the niche types. The niche with better survival in each comparison is shown in the color of the lines. The significance of whether tumors belonging to two niche types have different outcomes was determined by the Cox proportional hazard regression adjusted by tumor types. ***$p < 0.001$, **$p < 0.01$, *$p < 0.05$, .$p < 0.001$.

(B) The association of the niche types with the response to immunotherapy. The length of the diamonds represents the 95% confidence interval of arcsine transformed-rate difference (ASD) from meta-analysis.

(C) Forest plots showing the results of Niche_4 and Niche_13 from the single-cohort analysis and meta-analysis.

(D) Schematic of the classification of macrophages and stratification of patients by spatial distribution. Macrophages were classified into M01 (macrophages proximal to T cells) and M02 (macrophages proximal to tumor cells) based on their distance to tumor and T cells. Patients are divided into four groups based on the factions of M01 and M02 macrophages: G1: $M01^{hi}M02^{lo}$, G2: $M01^{hi}M02^{hi}$, G3: $M01^{lo}M02^{lo}$, and G4: $M01^{lo}M02^{hi}$.

(E) Representative samples of G1 and G4 from the multiplexed protein imaging datasets. (Left) *In situ* visualization of the markers. Scale bar, 30 μm. (Middle) Spatial distributions of tumor cells, macrophages, and T cells. (Right) Spatial distributions of M01 and M02.

(F) Kaplan-Meier survival plot for the four patient groups in NSCLC, HCC, and BRCA datasets. *p* values from log rank test and patient number of four groups are provided.

(G) Bar plot showing the distributions of patient subtypes in responders and non-responders to immunotherapy. *p* value by Fisher's exact test are to show the distribution difference of patients in four groups between responders and non-responders.

response to immunotherapy.[111] Another study on CRC revealed a C1QC+ macrophage-$CD4^+$ T cell niche was found in responders with immunotherapy.[112] In summary, we highlighted that the spatial distribution of macrophages is an important biomarker for patient prognosis and treatment response and has potential for clinical application in the future.

DISCUSSION

In this study, we dissected the TSME across different spatial extents, as "Cell types (one-cell resolution)-LCPs (TSME in spot level)-Niches (TSME in larger region)." Eventually, we identified 13 niches, which serve as conserved and fundamental spatial

Please cite this article in press as: Li et al., Pan-cancer analysis of spatial transcriptomics reveals heterogeneous tumor spatial microenvironment, Cell Reports Medicine (2026), https://doi.org/10.1016/j.xcrm.2026.102751

units in cancers (Table S12). We also identified complex niche-shared and niche-specific LR interactions, which are associated with the formation and function of the niches. Cell type-specific differential expression analysis indicates that expression of specific cell types varies among different niches, and this phenomenon may be related to either niche formation or neighboring cells. Extending the analysis to independent datasets with survival information and immunotherapy cohorts revealed that several niches are correlated with patient prognosis and response to immunotherapy.

Previously, pan-cancer studies on scRNA-seq have defined the recurrent cancer cell states and described the landscape of cellular heterogeneity within diverse cancer types.[26,85] However, the lack of spatial information makes it difficult to deduce how cancer cells interact with the tumor microenvironment in a spatial context to form organized systems. This question is addressed by our investigation of 373 spatial transcriptomics samples from 12 cancer types from the 10× Visium platform. Compared with other commercial platforms, the 10× Visium platform is most widely used, and there are a large number of public datasets available for data mining. However, emerging single-cell resolution spatial platforms (such as MERSCOPE and NanoString CosMx) only detect dozens of proteins or hundreds of genes relying on the designed panels. Such incompleteness makes it difficult to harmonize data from different sources and understand the gene programs of spatial organization. Therefore, currently 10× Visium platform is the most advantageous choice for understanding TSME from pan-cancer samples. A major limitation of 10× Visium data is that cell type abundances are estimated by computational deconvolution. For accuracy and robust estimation, we only considered common cell types with proper markers and ignored rare cell states. With the development of spatial technologies and the accumulation of single-cell-resolution public data, TSME of more refined cell subtypes would possibly be addressed in the future.

Integration analyses of pan-cancer spatial transcriptomics data are computationally challenging due to variability in samples, cancer types, and datasets. Therefore, we used consistent or optimal results if multiple methods are available and designed suitable strategies based on the analysis aim. To divide tissues from multiple cancer types into distinct tissue compartments, we developed a pipeline based on the information from deconvolution and CNV profiles, which is the fundamental process for TSME research. To combine the statistical results from multiple samples, we designed a rank-based meta-analysis method. Compared with previous methods that directly combine p values, our method takes the direction of the effects of each single sample into consideration and is less sensitive to the outliers. These improved computation methods enable our pan-cancer analysis of spatial transcriptomics data to obtain robust and reliable results.

A key finding of our research is the identification of consensus niches across diverse cancer types and their clinical significance. Specifically, Niche_13, which is mainly composed of cDC, CD4 T, and B cells, is associated with better survival and enhanced efficacy of immunotherapy. Another three niches contain macrophages, including Niche_4 (the colocalization of macrophages and tumor cells), Niche_10 (the colocalization of macrophages and stromal cells), and Niche_11 (the colocalization of macrophages and other immune cells, such as T cells and cDC). Data of spatial proteomics reveal that macrophages proximal to tumor cells are related to poorer survival and resistance to immunotherapy and macrophages proximal to T cells are related to better survival and response to immunotherapy. These findings suggest that macrophages play dual roles in both pro- and anti-tumor activities associated with their spatial distribution. As for the molecular mechanisms, different LR interactions were observed. Pro-tumoral IL1B-IL1R2 occurs in Niche_4, while immune-activated CXCL16-CXCR6 and IL15-IL15RA + IL2RB occur in Niche_11. The tumor cells in Niche_4 have higher expression of epithelial senescence-related genes, and the macrophages in Niche_11 have higher expression of immune-related genes than those in Niche_4 and Niche_10. These molecular features would be potential drug target for therapy. Further investigations are needed. Since our results have demonstrated that TSME is related to patient survival and response to treatment, improved experimental and computational technologies to quantify the TSME as biomarkers are needed to fit in with the clinical application, which helps with clinical decision. Moreover, the causal mechanism driving the TSME formation and the effect on tumor remain to be fully elucidated, which will help with the development of new therapeutic strategies.

In conclusion, our comprehensive analyses enhance the current understanding of the spatial microenvironment from a pan-cancer perspective and offer a valuable resource for future clinically or mechanistically oriented studies.

Limitations of the study

There are also several limitations to this study. First, the 10× Visium technology measures multi-cell spots and it is difficult to identify niche of fine-grained cell subtypes and microscopic tissue structures like blood vessels. With the accumulation of data from single-cell spatial technology, these problems will be better addressed. Second, the analysis of LR interactions may be affected by data sparsity, inter-patient heterogeneity, and coexpressed genes on multiple cell types. Deeper studies are needed to elucidate the underlying molecular mechanisms of niches. Third, the clinical relevance of spatial niches needs to be further investigated in larger cohorts with spatial transcriptome and prognostic information.

RESOURCE AVAILABILITY

Lead contact

Further information and requests should be directed to and will be fulfilled by the lead contact, Hong Li (lihong01@sinh.ac.cn).

Materials availability

This study did not generate new unique reagents.

Data and code availability

The spatial transcriptomics, scRNA-seq, bulk RNA-seq, and multiplexed imaging datasets in this study are provided in Table S1, along with the download links. Other processed data of spatial transcriptomics could be found in Zenodo (https://zenodo.org/records/18851187). The codes used for data analyses are available from GitHub (https://github.com/LiHongCSBLab/SpatialOmics_PanCancer). Any additional information required to reanalyze the data reported in this work is available from the lead contact upon request.

Please cite this article in press as: Li et al., Pan-cancer analysis of spatial transcriptomics reveals heterogeneous tumor spatial microenvironment, Cell Reports Medicine (2026), https://doi.org/10.1016/j.xcrm.2026.102751

CellPress
OPEN ACCESS

ACKNOWLEDGMENTS

This research was supported by the Noncommunicable Chronic Diseases-National Science and Technology Major Project (2024ZD0531300), National Natural Science Foundation of China (32300555 and 32470707), and Shanghai Municipal Science and Technology Major Project.

We acknowledge Yongqiang Gu, Weihong Sun (from Shanghai Institute of Nutrition and Health, Chinese Academy of Sciences), and Hong Wang (from College of Life Science and Technology, Jinan University) for their help with the biological interpretation of the results.

AUTHOR CONTRIBUTIONS

J.L., P.L., and H.L. contributed to the initial conceptualization and design of the project. P.L. and H.L. provided main resources and fundings. J.L. developed the method of the project. J.L. and Z.T. collected the public datasets. J.L. conducted most of the bioinformatic analysis, with the help of H.W., Z.T., X.Y., X.C., and J.Y. P.L. and W.C. helped with the visualization. J.L. wrote the manuscript, and it was revised by Z.T., P.L., and H.L. H.L. supervised the project. All the authors read and approved the final manuscript.

DECLARATION OF INTERESTS

The authors declare no competing interests.

DECLARATION OF GENERATIVE AI AND AI-ASSISTED TECHNOLOGIES IN THE WRITING PROCESS

During the preparation of this work DeepSeek and Qwen were used to help with language polishing. After using the tools, the authors reviewed and edited the content as needed and take full responsibility for the content of the publication.

STAR★METHODS

Detailed methods are provided in the online version of this paper and include the following:

- KEY RESOURCES TABLE
- METHOD DETAILS
  - Pan-cancer spatial transcriptomics data and preprocessing
  - Cell type deconvolution of 10× visium datasets
  - Identification of tissue compartments
  - Characterization of LCPs in malignant and stromal compartments
  - Connectivity score of the compartments
  - Unraveling the spatial distribution pattern of LCPs
  - Characterization of consensus niches
  - Identifying niches using subcellular resolved spatial transcriptomics datasets
  - Measurement of intra-tumor and inter-tumor heterogeneity
  - Meta analysis by combining the rank of P-values
  - Niche-related LR interactions across samples
  - Determination of the NCDEGs
  - Clinical implications of niches using bulk RNA-Seq datasets
  - Clinical implications of the spatial distribution of macrophages using multiplexed protein imaging data
- QUANTIFICATION AND STATISTICAL ANALYSIS

SUPPLEMENTAL INFORMATION

Supplemental information can be found online at https://doi.org/10.1016/j.xcrm.2026.102751.

Received: October 8, 2025
Revised: January 30, 2026
Accepted: March 18, 2026

REFERENCES

1. Anderson, N.M., and Simon, M.C. (2020). The tumor microenvironment. Curr. Biol. *30*, R921–R925. https://doi.org/10.1016/j.cub.2020.06.081.
2. Gao, Y., Li, J., Cheng, W., Diao, T., Liu, H., Bo, Y., Liu, C., Zhou, W., Chen, M., Zhang, Y., et al. (2024). Cross-tissue human fibroblast atlas reveals myofibroblast subtypes with distinct roles in immune modulation. Cancer Cell *42*, 1764–1783.e10. https://doi.org/10.1016/j.ccell.2024.08.020.
3. Zheng, L., Qin, S., Si, W., Wang, A., Xing, B., Gao, R., Ren, X., Wang, L., Wu, X., Zhang, J., et al. (2021). Pan-cancer single-cell landscape of tumor-infiltrating T cells. Science *374*, abe6474. https://doi.org/10.1126/science.abe6474.
4. Cheng, S., Li, Z., Gao, R., Xing, B., Gao, Y., Yang, Y., Qin, S., Zhang, L., Ouyang, H., Du, P., et al. (2021). A pan-cancer single-cell transcriptional atlas of tumor infiltrating myeloid cells. Cell *184*, 792–809.e23. https://doi.org/10.1016/j.cell.2021.01.010.
5. Luca, B.A., Steen, C.B., Matusiak, M., Azizi, A., Varma, S., Zhu, C., Przybyl, J., Espín-Pérez, A., Diehn, M., Alizadeh, A.A., et al. (2021). Atlas of clinically distinct cell states and ecosystems across human solid tumors. Cell *184*, 5482–5496.e28. https://doi.org/10.1016/j.cell.2021.09.014.
6. Steen, C.B., Luca, B.A., Esfahani, M.S., Azizi, A., Sworder, B.J., Nabet, B.Y., Kurtz, D.M., Liu, C.L., Khameneh, F., Advani, R.H., et al. (2021). The landscape of tumor cell states and ecosystems in diffuse large B cell lymphoma. Cancer Cell *39*, 1422–1437.e10. https://doi.org/10.1016/j.ccell.2021.08.011.
7. Marx, V. (2021). Method of the Year: spatially resolved transcriptomics. Nat. Methods *18*, 9–14. https://doi.org/10.1038/s41592-020-01033-y.
8. Moses, L., and Pachter, L. (2022). Museum of spatial transcriptomics. Nat. Methods *19*, 534–546. https://doi.org/10.1038/s41592-022-01409-2.
9. Gong, D., Arbesfeld-Qiu, J.M., Perrault, E., Bae, J.W., and Hwang, W.L. (2024). Spatial oncology: Translating contextual biology to the clinic. Cancer Cell *42*, 1653–1675. https://doi.org/10.1016/j.ccell.2024.09.001.
10. Andersson, A., Larsson, L., Stenbeck, L., Salmén, F., Ehinger, A., Wu, S.Z., Al-Eryani, G., Roden, D., Swarbrick, A., Borg, Å., et al. (2021). Spatial deconvolution of HER2-positive breast cancer delineates tumor-associated cell type interactions. Nat. Commun. *12*, 6012. https://doi.org/10.1038/s41467-021-26271-2.
11. Meylan, M., Petitprez, F., Becht, E., Bougoüin, A., Pupier, G., Calvez, A., Giglioli, I., Verkarre, V., Lacroix, G., Verneau, J., et al. (2022). Tertiary lymphoid structures generate and propagate anti-tumor antibody-producing plasma cells in renal cell cancer. Immunity *55*, 527–541.e5. https://doi.org/10.1016/j.immuni.2022.02.001.
12. Yan, Y., Sun, D., Hu, J., Chen, Y., Sun, L., Yu, H., Xiong, Y., Huang, Z., Xia, H., Zhu, X., et al. (2025). Multi-omic profiling highlights factors associated with resistance to immuno-chemotherapy in non-small-cell lung cancer. Nat. Genet. *57*, 126–139. https://doi.org/10.1038/s41588-024-01998-y.
13. Matusiak, M., Hickey, J.W., van IJzendoorn, D.G.P., Lu, G., Kidziński, L., Zhu, S., Colburg, D.R.C., Luca, B., Phillips, D.J., Brubaker, S.W., et al. (2024). Spatially Segregated Macrophage Populations Predict Distinct Outcomes in Colon Cancer. Cancer Discov. *14*, 1418–1439. https://doi.org/10.1158/2159-8290.CD-23-1300.
14. Cords, L., Tietscher, S., Anzeneder, T., Langwieder, C., Rees, M., de Souza, N., and Bodenmiller, B. (2023). Cancer-associated fibroblast classification in single-cell and spatial proteomics data. Nat. Commun. *14*, 4294. https://doi.org/10.1038/s41467-023-39762-1.
15. Cords, L., Engler, S., Haberecker, M., Rüschoff, J.H., Moch, H., de Souza, N., and Bodenmiller, B. (2024). Cancer-associated fibroblast phenotypes are associated with patient outcome in non-small cell lung cancer. Cancer Cell *42*, 396–412.e5. https://doi.org/10.1016/j.ccell.2023.12.021.

16. Liu, Y., Sinjab, A., Min, J., Han, G., Paradiso, F., Zhang, Y., Wang, R., Pei, G., Dai, Y., Liu, Y., et al. (2025). Conserved spatial subtypes and cellular neighborhoods of cancer-associated fibroblasts revealed by single-cell spatial multi-omics. Cancer Cell *43*, 905–924.e6. https://doi.org/10.1016/j.ccell.2025.03.004.

17. Ma, C., Yang, C., Peng, A., Sun, T., Ji, X., Mi, J., Wei, L., Shen, S., and Feng, Q. (2023). Pan-cancer spatially resolved single-cell analysis reveals the crosstalk between cancer-associated fibroblasts and tumor microenvironment. Mol. Cancer *22*, 170. https://doi.org/10.1186/s12943-023-01876-x.

18. Du, Y., Shi, J., Wang, J., Xun, Z., Yu, Z., Sun, H., Bao, R., Zheng, J., Li, Z., and Ye, Y. (2024). Integration of Pan-Cancer Single-Cell and Spatial Transcriptomics Reveals Stromal Cell Features and Therapeutic Targets in Tumor Microenvironment. Cancer Res. *84*, 192–210. https://doi.org/10.1158/0008-5472.CAN-23-1418.

19. Shi, J., Wei, X., Xun, Z., Ding, X., Liu, Y., Liu, L., and Ye, Y. (2024). The Web-Based Portal SpatialTME Integrates Histological Images with Single-Cell and Spatial Transcriptomics to Explore the Tumor Microenvironment. Cancer Res. *84*, 1210–1220. https://doi.org/10.1158/0008-5472.CAN-23-2650.

20. Deng, Y., Chen, P., Xiao, J., Li, M., Shen, J., Qin, S., Jia, T., Li, C., Chang, A., Zhang, W., et al. (2024). SCAR: Single-cell and Spatially-resolved Cancer Resources. Nucleic Acids Res. *52*, D1407–D1417. https://doi.org/10.1093/nar/gkad753.

21. Erickson, A., He, M., Berglund, E., Marklund, M., Mirzazadeh, R., Schultz, N., Kvastad, L., Andersson, A., Bergenstråhle, L., Bergenstråhle, J., et al. (2022). Spatially resolved clonal copy number alterations in benign and malignant tissue. Nature *608*, 360–367. https://doi.org/10.1038/s41586-022-05023-2.

22. Hu, J., Wang, S.-G., Hou, Y., Chen, Z., Liu, L., Li, R., Li, N., Zhou, L., Yang, Y., Wang, L., et al. (2024). Multi-omic profiling of clear cell renal cell carcinoma identifies metabolic reprogramming associated with disease progression. Nat. Genet. *56*, 442–457. https://doi.org/10.1038/s41588-024-01662-5.

23. Davidson, G., Helleux, A., Vano, Y.A., Lindner, V., Fattori, A., Cerciat, M., Elaidi, R.T., Verkarre, V., Sun, C.-M., Chevreau, C., et al. (2023). Mesenchymal-like Tumor Cells and Myofibroblastic Cancer-Associated Fibroblasts Are Associated with Progression and Immunotherapy Response of Clear Cell Renal Cell Carcinoma. Cancer Res. *83*, 2952–2969. https://doi.org/10.1158/0008-5472.CAN-22-3034.

24. Liu, Y., Xun, Z., Ma, K., Liang, S., Li, X., Zhou, S., Sun, L., Liu, Y., Du, Y., Guo, X., et al. (2023). Identification of a tumour immune barrier in the HCC microenvironment that determines the efficacy of immunotherapy. J. Hepatol. *78*, 770–782. https://doi.org/10.1016/j.jhep.2023.01.011.

25. Mastering Biology to Advance Human Health 10x Genomics. https://www.10xgenomics.com/.

26. Barkley, D., Moncada, R., Pour, M., Liberman, D.A., Dryg, I., Werba, G., Wang, W., Baron, M., Rao, A., Xia, B., et al. (2022). Cancer cell states recur across tumor types and form specific interactions with the tumor microenvironment. Nat. Genet. *54*, 1192–1201. https://doi.org/10.1038/s41588-022-01141-9.

27. Wang, Y., Chen, D., Liu, Y., Shi, D., Duan, C., Li, J., Shi, X., Zhang, Y., Yu, Z., Sun, N., et al. (2023). Multidirectional characterization of cellular composition and spatial architecture in human multiple primary lung cancers. Cell Death Dis. *14*, 462. https://doi.org/10.1038/s41419-023-05992-w.

28. De Zuani, M., Xue, H., Park, J.S., Dentro, S.C., Seferbekova, Z., Tessier, J., Curras-Alonso, S., Hadjipanayis, A., Athanasiadis, E.I., Gerstung, M., et al. (2024). Single-cell and spatial transcriptomics analysis of non-small cell lung cancer. Nat. Commun. *15*, 4388. https://doi.org/10.1038/s41467-024-48700-8.

29. Zhu, J., Fan, Y., Xiong, Y., Wang, W., Chen, J., Xia, Y., Lei, J., Gong, L., Sun, S., and Jiang, T. (2022). Delineating the dynamic evolution from preneoplasia to invasive lung adenocarcinoma by integrating single-cell RNA sequencing and spatial transcriptomics. Exp. Mol. Med. *54*, 2060–2076. https://doi.org/10.1038/s12276-022-00896-9.

30. Wang, Y.F., Yuan, S.X., Jiang, H., Li, Z.X., Yin, H.Z., Tan, J., Dai, Z.H., Ge, C.M., Sun, S.H., and Yang, F. (2022). Spatial maps of hepatocellular carcinoma transcriptomes reveal spatial expression patterns in tumor immune microenvironment. Theranostics *12*, 4163–4180. https://doi.org/10.7150/thno.71873.

31. Wu, R., Guo, W., Qiu, X., Wang, S., Sui, C., Lian, Q., Wu, J., Shan, Y., Yang, Z., Yang, S., et al. (2021). Comprehensive analysis of spatial architecture in primary liver cancer. Sci. Adv. *7*, eabg3750. https://doi.org/10.1126/sciadv.abg3750.

32. Zhang, S., Yuan, L., Danilova, L., Mo, G., Zhu, Q., Deshpande, A., Bell, A.T.F., Elisseeff, J., Popel, A.S., Anders, R.A., et al. (2023). Spatial transcriptomics analysis of neoadjuvant cabozantinib and nivolumab in advanced hepatocellular carcinoma identifies independent mechanisms of resistance and recurrence. Genome Med. *15*, 72. https://doi.org/10.1186/s13073-023-01218-y.

33. Jing, S.Y., Liu, D., Feng, N., Dong, H., Wang, H.Q., Yan, X., Chen, X.F., Qu, M.C., Lin, P., Yi, B., et al. (2024). Spatial multiomics reveals a subpopulation of fibroblasts associated with cancer stemness in human hepatocellular carcinoma. Genome Med. *16*, 98. https://doi.org/10.1186/s13073-024-01367-8.

34. Wu, S.Z., Al-Eryani, G., Roden, D.L., Junankar, S., Harvey, K., Andersson, A., Thennavan, A., Wang, C., Torpy, J.R., Bartonicek, N., et al. (2021). A single-cell and spatially resolved atlas of human breast cancers. Nat. Genet. *53*, 1334–1347. https://doi.org/10.1038/s41588-021-00911-1.

35. Coutant, A., Cockenpot, V., Muller, L., Degletagne, C., Pommier, R., Tonon, L., Ardin, M., Michallet, M.-C., Caux, C., Laurent, M., et al. (2023). Spatial Transcriptomics Reveal Pitfalls and Opportunities for the Detection of Rare High-Plasticity Breast Cancer Subtypes. Lab. Invest. *103*, 100258. https://doi.org/10.1016/j.labinv.2023.100258.

36. Zhao, E., Stone, M.R., Ren, X., Guenthoer, J., Smythe, K.S., Pulliam, T., Williams, S.R., Uytingco, C.R., Taylor, S.E.B., Nghiem, P., et al. (2021). Spatial transcriptomics at subspot resolution with BayesSpace. Nat. Biotechnol. *39*, 1375–1384. https://doi.org/10.1038/s41587-021-00935-2.

37. Bassiouni, R., Idowu, M.O., Gibbs, L.D., Robila, V., Grizzard, P.J., Webb, M.G., Song, J., Noriega, A., Craig, D.W., and Carpten, J.D. (2023). Spatial Transcriptomic Analysis of a Diverse Patient Cohort Reveals a Conserved Architecture in Triple-Negative Breast Cancer. Cancer Res. *83*, 34–48. https://doi.org/10.1158/0008-5472.CAN-22-2682.

38. Liu, Y.-M., Ge, J.-Y., Chen, Y.-F., Liu, T., Chen, L., Liu, C.-C., Ma, D., Chen, Y.-Y., Cai, Y.-W., Xu, Y.-Y., et al. (2023). Combined Single-Cell and Spatial Transcriptomics Reveal the Metabolic Evolvement of Breast Cancer during Early Dissemination. Adv. Sci. *10*, 2205395. https://doi.org/10.1002/advs.202205395.

39. Ravi, V.M., Will, P., Kueckelhaus, J., Sun, N., Joseph, K., Salié, H., Vollmer, L., Kuliesiute, U., von Ehr, J., Benotmane, J.K., et al. (2022). Spatially resolved multi-omics deciphers bidirectional tumor-host interdependence in glioblastoma. Cancer Cell *40*, 639–655.e13. https://doi.org/10.1016/j.ccell.2022.05.009.

40. Ren, Y., Huang, Z., Zhou, L., Xiao, P., Song, J., He, P., Xie, C., Zhou, R., Li, M., Dong, X., et al. (2023). Spatial transcriptomics reveals niche-specific enrichment and vulnerabilities of radial glial stem-like cells in malignant gliomas. Nat. Commun. *14*, 1028. https://doi.org/10.1038/s41467-023-36707-6.

41. Mei, Y., Wang, X., Zhang, J., Liu, D., He, J., Huang, C., Liao, J., Wang, Y., Feng, Y., Li, H., et al. (2023). Siglec-9 acts as an immune-checkpoint molecule on macrophages in glioblastoma, restricting T-cell priming and immunotherapy response. Nat. Cancer *4*, 1273–1291. https://doi.org/10.1038/s43018-023-00598-9.

42. Al-Dalahmah, O., Argenziano, M.G., Kannan, A., Mahajan, A., Furnari, J., Paryani, F., Boyett, D., Save, A., Humala, N., Khan, F., et al. (2023). Reconvolving the compositional landscape of primary and recurrent

glioblastoma reveals prognostic and targetable tissue states. Nat. Commun. *14*, 2586. https://doi.org/10.1038/s41467-023-38186-1.

43. Li, R., Ferdinand, J.R., Loudon, K.W., Bowyer, G.S., Laidlaw, S., Muyas, F., Mamanova, L., Neves, J.B., Bolt, L., Fasouli, E.S., et al. (2022). Mapping single-cell transcriptomes in the intra-tumoral and associated territories of kidney cancer. Cancer Cell *40*, 1583–1599.e10. https://doi.org/10.1016/j.ccell.2022.11.001.

44. Wu, Y., Terekhanova, N.V., Caravan, W., Naser Al Deen, N., Lal, P., Chen, S., Mo, C.-K., Cao, S., Li, Y., Karpova, A., et al. (2023). Epigenetic and transcriptomic characterization reveals progression markers and essential pathways in clear cell renal cell carcinoma. Nat. Commun. *14*, 1681. https://doi.org/10.1038/s41467-023-37211-7.

45. Ozato, Y., Kojima, Y., Kobayashi, Y., Hisamatsu, Y., Toshima, T., Yonemura, Y., Masuda, T., Kagawa, K., Goto, Y., Utou, M., et al. (2023). Spatial and single-cell transcriptomics decipher the cellular environment containing HLA-G+ cancer cells and SPP1+ macrophages in colorectal cancer. Cell Rep. *42*, 111929. https://doi.org/10.1016/j.celrep.2022.111929.

46. Qi, J., Sun, H., Zhang, Y., Wang, Z., Xun, Z., Li, Z., Ding, X., Bao, R., Hong, L., Jia, W., et al. (2022). Single-cell and spatial analysis reveal interaction of FAP+ fibroblasts and SPP1+ macrophages in colorectal cancer. Nat. Commun. *13*, 1742. https://doi.org/10.1038/s41467-022-29366-6.

47. Valdeolivas, A., Amberg, B., Giroud, N., Richardson, M., Gálvez, E.J.C., Badillo, S., Julien-Laferrière, A., Túrós, D., Voith von Voithenberg, L., Wells, I., et al. (2024). Profiling the heterogeneity of colorectal cancer consensus molecular subtypes using spatial transcriptomics. npj Precis. Oncol. *8*, 10. https://doi.org/10.1038/s41698-023-00488-4.

48. Wang, F., Long, J., Li, L., Wu, Z.-X., Da, T.-T., Wang, X.-Q., Huang, C., Jiang, Y.-H., Yao, X.-Q., Ma, H.-Q., et al. (2023). Single-cell and spatial transcriptome analysis reveals the cellular heterogeneity of liver metastatic colorectal cancer. Sci. Adv. *9*, eadf5464. https://doi.org/10.1126/sciadv.adf5464.

49. Park, S.S., Lee, Y.-K., Choi, Y.W., Lim, S.B., Park, S.H., Kim, H.K., Shin, J.S., Kim, Y.H., Lee, D.H., Kim, J.-H., and Park, T.J. (2024). Cellular senescence is associated with the spatial evolution toward a higher metastatic phenotype in colorectal cancer. Cell Rep. *43*, 113912. https://doi.org/10.1016/j.celrep.2024.113912.

50. Heiser, C.N., Simmons, A.J., Revetta, F., McKinley, E.T., Ramirez-Solano, M.A., Wang, J., Kaur, H., Shao, J., Ayers, G.D., Wang, Y., et al. (2023). Molecular cartography uncovers evolutionary and microenvironmental dynamics in sporadic colorectal tumors. Cell *186*, 5620–5637.e16. https://doi.org/10.1016/j.cell.2023.11.006.

51. Gracia Villacampa, E., Larsson, L., Mirzazadeh, R., Kvastad, L., Andersson, A., Mollbrink, A., Kokaraki, G., Monteil, V., Schultz, N., Appelberg, K.S., et al. (2021). Genome-wide spatial expression profiling in formalin-fixed tissues. Cell Genom. *1*, 100065. https://doi.org/10.1016/j.xgen.2021.100065.

52. Denisenko, E., de Kock, L., Tan, A., Beasley, A.B., Beilin, M., Jones, M.E., Hou, R., Muirí, D.Ó., Bilic, S., Mohan, G.R.K.A., et al. (2024). Spatial transcriptomics reveals discrete tumour microenvironments and autocrine loops within ovarian cancer subclones. Nat. Commun. *15*, 2860. https://doi.org/10.1038/s41467-024-47271-y.

53. Lyubetskaya, A., Rabe, B., Fisher, A., Lewin, A., Neuhaus, I., Brett, C., Brett, T., Pereira, E., Golhar, R., Kebede, S., et al. (2022). Assessment of spatial transcriptomics for oncology discovery. Cell Rep. Methods *2*, 100340. https://doi.org/10.1016/j.crmeth.2022.100340.

54. Sans, M., Makino, Y., Min, J., Rajapakshe, K.I., Yip-Schneider, M., Schmidt, C.M., Hurd, M.W., Burks, J.K., Gomez, J.A., Thege, F.I., et al. (2023). Spatial Transcriptomics of Intraductal Papillary Mucinous Neoplasms of the Pancreas Identifies NKX6-2 as a Driver of Gastric Differentiation and Indolent Biological Potential. Cancer Discov. *13*, 1844–1861. https://doi.org/10.1158/2159-8290.CD-22-1200.

55. Yousuf, S., Qiu, M., Voith von Voithenberg, L., Hulkkonen, J., Macinkovic, I., Schulz, A.R., Hartmann, D., Mueller, F., Mijatovic, M., Ibberson, D., et al. (2023). Spatially Resolved Multi-Omics Single-Cell Analyses Inform Mechanisms of Immune Dysfunction in Pancreatic Cancer. Gastroenterology *165*, 891–908.e14. https://doi.org/10.1053/j.gastro.2023.05.036.

56. Cui Zhou, D., Jayasinghe, R.G., Chen, S., Herndon, J.M., Iglesia, M.D., Navale, P., Wendl, M.C., Caravan, W., Sato, K., Storrs, E., et al. (2022). Spatially restricted drivers and transitional cell populations cooperate with the microenvironment in untreated and chemo-resistant pancreatic cancer. Nat. Genet. *54*, 1390–1405. https://doi.org/10.1038/s41588-022-01157-1.

57. Nieto, P., Elosua-Bayes, M., Trincado, J.L., Marchese, D., Massoni-Badosa, R., Salvany, M., Henriques, A., Nieto, J., Aguilar-Fernández, S., Mereu, E., et al. (2021). A single-cell tumor immune atlas for precision oncology. Genome Res. *31*, 1913–1926. https://doi.org/10.1101/gr.273300.120.

58. Arora, R., Cao, C., Kumar, M., Sinha, S., Chanda, A., McNeil, R., Samuel, D., Arora, R.K., Matthews, T.W., Chandarana, S., et al. (2023). Spatial transcriptomics reveals distinct and conserved tumor core and edge architectures that predict survival and targeted therapy response. Nat. Commun. *14*, 5029. https://doi.org/10.1038/s41467-023-40271-4.

59. Ji, A.L., Rubin, A.J., Thrane, K., Jiang, S., Reynolds, D.L., Meyers, R.M., Guo, M.G., George, B.M., Mollbrink, A., Bergenstråhle, J., et al. (2020). Multimodal Analysis of Composition and Spatial Architecture in Human Squamous Cell Carcinoma. Cell *182*, 497–514.e22. https://doi.org/10.1016/j.cell.2020.05.039.

60. Bergenstråhle, L., He, B., Bergenstråhle, J., Abalo, X., Mirzazadeh, R., Thrane, K., Ji, A.L., Andersson, A., Larsson, L., Stakenborg, N., et al. (2022). Super-resolved spatial transcriptomics by deep data fusion. Nat. Biotechnol. *40*, 476–479. https://doi.org/10.1038/s41587-021-01075-3.

61. Cheng, H.-Y., Hsieh, C.-H., Lin, P.-H., Chen, Y.-T., Hsu, D.S.-S., Tai, S.-K., Chu, P.-Y., and Yang, M.-H. (2022). Snail-regulated exosomal microRNA-21 suppresses NLRP3 inflammasome activity to enhance cisplatin resistance. J. Immunother. Cancer *10*, e004832. https://doi.org/10.1136/jitc-2022-004832.

62. Cable, D.M., Murray, E., Zou, L.S., Goeva, A., Macosko, E.Z., Chen, F., and Irizarry, R.A. (2022). Robust decomposition of cell type mixtures in spatial transcriptomics. Nat. Biotechnol. *40*, 517–526. https://doi.org/10.1038/s41587-021-00830-w.

63. Spatial immune profiling defines a subset of human gliomas with functional tertiary lymphoid structures (2025). Immunity 58, 2847-2863.e8. https://doi.org/10.1016/j.immuni.2025.09.018.

64. Thorsson, V., Gibbs, D.L., Brown, S.D., Wolf, D., Bortone, D.S., Ou Yang, T.-H., Porta-Pardo, E., Gao, G.F., Plaisier, C.L., Eddy, J.A., et al. (2018). The Immune Landscape of Cancer. Immunity *48*, 812–830.e14. https://doi.org/10.1016/j.immuni.2018.03.023.

65. Gibbs, D.L. (2020). Robust classification of Immune Subtypes in Cancer. Preprint at bioRxiv. https://doi.org/10.1101/2020.01.17.910950.

66. Romańczyk, W., and Pryczynicz, A. (2025). The Significance of Nectin Family Proteins in Various Cancerogenous Processes. Int. J. Mol. Sci. *26*, 3200. https://doi.org/10.3390/ijms26073200.

67. Kobecki, J., Gajdzis, P., Mazur, G., and Chabowski, M. (2022). Nectins and Nectin-like Molecules in Colorectal Cancer: Role in Diagnostics, Prognostic Values, and Emerging Treatment Options: A Literature Review. Diagnostics *12*, 3076. https://doi.org/10.3390/diagnostics12123076.

68. Wu, X., Qian, L., Zhao, H., Lei, W., Liu, Y., Xu, X., Li, J., Yang, Z., Wang, D., Zhang, Y., et al. (2023). CXCL12/CXCR4: An amazing challenge and opportunity in the fight against fibrosis. Ageing Res. Rev. *83*, 101809. https://doi.org/10.1016/j.arr.2022.101809.

69. Liang, Z., Brooks, J., Willard, M., Liang, K., Yoon, Y., Kang, S., and Shim, H. (2007). CXCR4/CXCL12 axis promotes VEGF-mediated tumor angiogenesis through Akt signaling pathway. Biochem. Biophys. Res. Commun. *359*, 716–722. https://doi.org/10.1016/j.bbrc.2007.05.182.

70. Heidegger, I., Fotakis, G., Offermann, A., Goveia, J., Daum, S., Salcher, S., Noureen, A., Timmer-Bosscha, H., Schäfer, G., Walenkamp, A., et al. (2022). Comprehensive characterization of the prostate tumor microenvironment identifies CXCR4/CXCL12 crosstalk as a novel antiangiogenic therapeutic target in prostate cancer. Mol. Cancer *21*, 132. https://doi.org/10.1186/s12943-022-01597-7.

71. Hornburg, M., Desbois, M., Lu, S., Guan, Y., Lo, A.A., Kaufman, S., Elrod, A., Lotstein, A., DesRochers, T.M., Munoz-Rodriguez, J.L., et al. (2021). Single-cell dissection of cellular components and interactions shaping the tumor immune phenotypes in ovarian cancer. Cancer Cell *39*, 928–944.e6. https://doi.org/10.1016/j.ccell.2021.04.004.

72. Xia, Y., Sun, T., Li, G., Li, M., Wang, D., Su, X., Ye, J., and Ji, C. (2023). Spatial single cell analysis of tumor microenvironment remodeling pattern in primary central nervous system lymphoma. Leukemia *37*, 1499–1510. https://doi.org/10.1038/s41375-023-01908-x.

73. Marcovecchio, P.M., Thomas, G., and Salek-Ardakani, S. (2021). CXCL9-expressing tumor-associated macrophages: new players in the fight against cancer. J. Immunother. Cancer *9*, e002045. https://doi.org/10.1136/jitc-2020-002045.

74. Litchfield, K., Reading, J.L., Puttick, C., Thakkar, K., Abbosh, C., Bentham, R., Watkins, T.B.K., Rosenthal, R., Biswas, D., Rowan, A., et al. (2021). Meta-analysis of tumor- and T cell-intrinsic mechanisms of sensitization to checkpoint inhibition. Cell *184*, 596–614.e14. https://doi.org/10.1016/j.cell.2021.01.002.

75. Yang, J., Liu, Q., and Shyr, Y. (2024). A Large-Scale Meta-Analysis Reveals Positive Feedback between Macrophages and T Cells That Sensitizes Tumors to Immunotherapy. Cancer Res. *84*, 626–638. https://doi.org/10.1158/0008-5472.CAN-23-2006.

76. Schumacher, T.N., and Thommen, D.S. (2022). Tertiary lymphoid structures in cancer. Science *375*, eabf9419. https://doi.org/10.1126/science.abf9419.

77. Teillaud, J.-L., Houel, A., Panouillot, M., Riffard, C., and Dieu-Nosjean, M.-C. (2024). Tertiary lymphoid structures in anticancer immunity. Nat. Rev. Cancer *24*, 629–646. https://doi.org/10.1038/s41568-024-00728-0.

78. Eum, H.H., Kwon, M., Ryu, D., Jo, A., Chung, W., Kim, N., Hong, Y., Son, D.-S., Kim, S.T., Lee, J., et al. (2020). Tumor-promoting macrophages prevail in malignant ascites of advanced gastric cancer. Exp. Mol. Med. *52*, 1976–1988. https://doi.org/10.1038/s12276-020-00538-y.

79. Caronni, N., La Terza, F., Vittoria, F.M., Barbiera, G., Mezzanzanica, L., Cuzzola, V., Barresi, S., Pellegatta, M., Canevazzi, P., Dunsmore, G., et al. (2023). IL-1β+ macrophages fuel pathogenic inflammation in pancreatic cancer. Nature *623*, 415–422. https://doi.org/10.1038/s41586-023-06685-2.

80. Mapping single-cell transcriptomes in the intra-tumoral and associated territories of kidney cancer (2022). Cancer Cell 40, 1583-1599.e10. https://doi.org/10.1016/j.ccell.2022.11.001.

81. Kureshi, C.T., and Dougan, S.K. (2025). Cytokines in cancer. Cancer Cell *43*, 15–35. https://doi.org/10.1016/j.ccell.2024.11.011.

82. Shrager, S.H., and Kiel, C. (2020). SnapShot: APC/T Cell Immune Checkpoints. Cell *183*, 1142–1142.e1. https://doi.org/10.1016/j.cell.2020.10.007.

83. Paterson, A.M., Vanguri, V.K., and Sharpe, A.H. (2009). SnapShot: B7/CD28 Costimulation. Cell *137*, 974-4.e1. https://doi.org/10.1016/j.cell.2009.05.015.

84. Kraehenbuehl, L., Weng, C.-H., Eghbali, S., Wolchok, J.D., and Merghoub, T. (2022). Enhancing immunotherapy in cancer by targeting emerging immunomodulatory pathways. Nat. Rev. Clin. Oncol. *19*, 37–50. https://doi.org/10.1038/s41571-021-00552-7.

85. Gavish, A., Tyler, M., Greenwald, A.C., Hoefflin, R., Simkin, D., Tschernichovsky, R., Galili Darnell, N., Somech, E., Barbolin, C., Antman, T., et al. (2023). Hallmarks of transcriptional intratumour heterogeneity across a thousand tumours. Nature *618*, 598–606. https://doi.org/10.1038/s41586-023-06130-4.

86. Jorgovanovic, D., Song, M., Wang, L., and Zhang, Y. (2020). Roles of IFN-γ in tumor progression and regression: a review. Biomark. Res. *8*, 49. https://doi.org/10.1186/s40364-020-00228-x.

87. Okada, Y., Takahashi, N., Takayama, T., and Goel, A. (2021). LAMC2 promotes cancer progression and gemcitabine resistance through modulation of EMT and ATP-binding cassette transporters in pancreatic ductal adenocarcinoma. Carcinogenesis *42*, 546–556. https://doi.org/10.1093/carcin/bgab011.

88. Liu, M., Cai, R., Wang, T., Yang, X., Wang, M., Kuang, Z., Xie, Y., Zhang, J., and Zheng, Y. (2021). LAMC2 promotes the proliferation of cancer cells and induce infiltration of macrophages in non-small cell lung cancer. Ann. Transl. Med. *9*, 1392. https://doi.org/10.21037/atm-21-4507.

89. Morales-Valencia, J., Lau, L., Martí-Nin, T., Ozerdem, U., and David, G. (2022). Therapy-induced senescence promotes breast cancer cells plasticity by inducing Lipocalin-2 expression. Oncogene *41*, 4361–4370. https://doi.org/10.1038/s41388-022-02433-4.

90. Jiang, S.-Y., Tian, T., Yao, H., Xia, X.-M., Wang, C., Cao, L., Hu, G., Du, R.-H., and Lu, M. (2023). The cGAS-STING-YY1 axis accelerates progression of neurodegeneration in a mouse model of Parkinson's disease via LCN2-dependent astrocyte senescence. Cell Death Differ. *30*, 2280–2292. https://doi.org/10.1038/s41418-023-01216-y.

91. Chi, Y., Remsik, J., Kiseliovas, V., Derderian, C., Sener, U., Alghader, M., Saadeh, F., Nikishina, K., Bale, T., Iacobuzio-Donahue, C., et al. (2020). Cancer cells deploy lipocalin-2 to collect limiting iron in leptomeningeal metastasis. Science *369*, 276–282. https://doi.org/10.1126/science.aaz2193.

92. Coulton, A., Murai, J., Qian, D., Thakkar, K., Lewis, C.E., and Litchfield, K. (2024). Using a pan-cancer atlas to investigate tumour associated macrophages as regulators of immunotherapy response. Nat. Commun. *15*, 5665. https://doi.org/10.1038/s41467-024-49885-8.

93. Chen, K., Li, Y., Ni, J., Yang, X., Zhou, Y., Pang, Y., Ye, R., Chen, H., Yu, S., Wang, P., and Zhu, Z. (2024). Identification of a novel subtype of SPP1 + macrophages expressing SIRPα: implications for tumor immune evasion and treatment response prediction. Exp. Hematol. Oncol. *13*, 119. https://doi.org/10.1186/s40164-024-00587-3.

94. Guinney, J., Dienstmann, R., Wang, X., de Reyniès, A., Schlicker, A., Soneson, C., Marisa, L., Roepman, P., Nyamundanda, G., Angelino, P., et al. (2015). The consensus molecular subtypes of colorectal cancer. Nat. Med. *21*, 1350–1356. https://doi.org/10.1038/nm.3967.

95. Cancer Genome Atlas Network (2015). Comprehensive genomic characterization of head and neck squamous cell carcinomas. Nature *517*, 576–582. https://doi.org/10.1038/nature14129.

96. Cancer Genome Atlas Research Network Electronic address wheeler@bcm edu; Cancer Genome Atlas Research Network (2017). Electronic address: wheeler@bcm.edu and Cancer Genome Atlas Research Network (2017). Comprehensive and Integrative Genomic Characterization of Hepatocellular Carcinoma. Cell *169*, 1327–1341.e23. https://doi.org/10.1016/j.cell.2017.05.046.

97. Cancer Genome Atlas Research Network (2013). Comprehensive molecular characterization of clear cell renal cell carcinoma. Nature *499*, 43–49. https://doi.org/10.1038/nature12222.

98. Hutter, C., and Zenklusen, J.C. (2018). The Cancer Genome Atlas: Creating Lasting Value beyond Its Data. Cell *173*, 283–285. https://doi.org/10.1016/j.cell.2018.03.042.

99. Kang, J., Lee, J.H., Cha, H., An, J., Kwon, J., Lee, S., Kim, S., Baykan, M.Y., Kim, S.Y., An, D., et al. (2024). Systematic dissection of tumor-normal single-cell ecosystems across a thousand tumors of 30 cancer types. Nat. Commun. *15*, 4067. https://doi.org/10.1038/s41467-024-48310-4.

100. Hu, J., Zhang, L., Xia, H., Yan, Y., Zhu, X., Sun, F., Sun, L., Li, S., Li, D., Wang, J., et al. (2023). Tumor microenvironment remodeling after neoadjuvant immunotherapy in non-small cell lung cancer revealed by single-cell RNA sequencing. Genome Med. *15*, 14. https://doi.org/10.1186/s13073-023-01164-9.

101. Miao, D., Margolis, C.A., Gao, W., Voss, M.H., Li, W., Martini, D.J., Norton, C., Bossé, D., Wankowicz, S.M., Cullen, D., et al. (2018). Genomic correlates of response to immune checkpoint therapies in clear cell renal cell carcinoma. Science *359*, 801–806. https://doi.org/10.1126/science.aan5951.

102. Hwang, S., Kwon, A.-Y., Jeong, J.-Y., Kim, S., Kang, H., Park, J., Kim, J.-H., Han, O.J., Lim, S.M., and An, H.J. (2020). Immune gene signatures for predicting durable clinical benefit of anti-PD-1 immunotherapy in patients with non-small cell lung cancer. Sci. Rep. *10*, 643. https://doi.org/10.1038/s41598-019-57218-9.

103. Braun, D.A., Hou, Y., Bakouny, Z., Ficial, M., Sant' Angelo, M., Forman, J., Ross-Macdonald, P., Berger, A.C., Jegede, O.A., Elagina, L., et al. (2020). Interplay of somatic alterations and immune infiltration modulates response to PD-1 blockade in advanced clear cell renal cell carcinoma. Nat. Med. *26*, 909–918. https://doi.org/10.1038/s41591-020-0839-y.

104. Markowski, M.C., Taplin, M.-E., Aggarwal, R., Sena, L.A., Wang, H., Qi, H., Lalji, A., Sinibaldi, V., Carducci, M.A., Paller, C.J., et al. (2024). Bipolar androgen therapy plus nivolumab for patients with metastatic castration-resistant prostate cancer: the COMBAT phase II trial. Nat. Commun. *15*, 14. https://doi.org/10.1038/s41467-023-44514-2.

105. Ravi, A., Hellmann, M.D., Arniella, M.B., Holton, M., Freeman, S.S., Naranbhai, V., Stewart, C., Leshchiner, I., Kim, J., Akiyama, Y., et al. (2023). Genomic and transcriptomic analysis of checkpoint blockade response in advanced non-small cell lung cancer. Nat. Genet. *55*, 807–819. https://doi.org/10.1038/s41588-023-01355-5.

106. Giesen, C., Wang, H.A.O., Schapiro, D., Zivanovic, N., Jacobs, A., Hattendorf, B., Schüffler, P.J., Grolimund, D., Buhmann, J.M., Brandt, S., et al. (2014). Highly multiplexed imaging of tumor tissues with subcellular resolution by mass cytometry. Nat. Methods *11*, 417–422. https://doi.org/10.1038/nmeth.2869.

107. Y, G., N, S., J, K.-D., S, B., M, H., G, V., S, B., and Gp, N. (2018). Deep Profiling of Mouse Splenic Architecture with CODEX Multiplexed Imaging. Cell *174*. https://doi.org/10.1016/j.cell.2018.07.010.

108. Qiu, X., Zhou, T., Li, S., Wu, J., Tang, J., Ma, G., Yang, S., Hu, J., Wang, K., Shen, S., et al. (2024). Spatial single-cell protein landscape reveals vimentinhigh macrophages as immune-suppressive in the microenvironment of hepatocellular carcinoma. Nat. Cancer *5*, 1557–1578. https://doi.org/10.1038/s43018-024-00824-y.

109. Danenberg, E., Bardwell, H., Zanotelli, V.R.T., Provenzano, E., Chin, S.-F., Rueda, O.M., Green, A., Rakha, E., Aparicio, S., Ellis, I.O., et al. (2022). Breast tumor microenvironment structures are associated with genomic features and clinical outcome. Nat. Genet. *54*, 660–669. https://doi.org/10.1038/s41588-022-01041-y.

110. Xiao, X., Guo, Q., Cui, C., Lin, Y., Zhang, L., Ding, X., Li, Q., Wang, M., Yang, W., Kong, Y., and Yu, R. (2022). Multiplexed imaging mass cytometry reveals distinct tumor-immune microenvironments linked to immunotherapy responses in melanoma. Commun. Med. *2*, 131. https://doi.org/10.1038/s43856-022-00197-2.

111. Chen, H., Deng, C., Gao, J., Wang, J., Fu, F., Wang, Y., Wang, Q., Zhang, M., Zhang, S., Fan, F., et al. (2025). Integrative spatial analysis reveals tumor heterogeneity and immune colony niche related to clinical outcomes in small cell lung cancer. Cancer Cell *43*, 519–536.e5. https://doi.org/10.1016/j.ccell.2025.01.012.

112. Zhang, H., Hong, L., Dong, Z., Xin, S., Lin, B., Cheng, J., Tian, W., Li, B., Wang, J., Liu, X., et al. (2025). Spatially resolved C1QC+ macrophage-CD4+ T cell niche in colorectal cancer microenvironment: implications for immunotherapy response. Cell Discov. *11*, 60. https://doi.org/10.1038/s41421-025-00811-2.

113. Qian, J., Olbrecht, S., Boeckx, B., Vos, H., Laoui, D., Etlioglu, E., Wauters, E., Pomella, V., Verbandt, S., Busschaert, P., et al. (2020). A pan-cancer blueprint of the heterogeneous tumor microenvironment revealed by single-cell profiling. Cell Res. *30*, 745–762. https://doi.org/10.1038/s41422-020-0355-0.

114. Lee, H.-O., Hong, Y., Etlioglu, H.E., Cho, Y.B., Pomella, V., Van den Bosch, B., Vanhecke, J., Verbandt, S., Hong, H., Min, J.-W., et al. (2020). Lineage-dependent gene expression programs influence the immune landscape of colorectal cancer. Nat. Genet. *52*, 594–603. https://doi.org/10.1038/s41588-020-0636-z.

115. Lu, Y., Yang, A., Quan, C., Pan, Y., Zhang, H., Li, Y., Gao, C., Lu, H., Wang, X., Cao, P., et al. (2022). A single-cell atlas of the multicellular ecosystem of primary and metastatic hepatocellular carcinoma. Nat. Commun. *13*, 4594. https://doi.org/10.1038/s41467-022-32283-3.

116. Vázquez-García, I., Uhlitz, F., Ceglia, N., Lim, J.L.P., Wu, M., Mohibullah, N., Niyazov, J., Ruiz, A.E.B., Boehm, K.M., Bojilova, V., et al. (2022). Ovarian cancer mutational processes drive site-specific immune evasion. Nature *612*, 778–786. https://doi.org/10.1038/s41586-022-05496-1.

117. Ruiz-Moreno, C., Salas, S.M., Samuelsson, E., Brandner, S., Kranendonk, M.E.G., Nilsson, M., and Stunnenberg, H.G. (2022). Harmonized single-cell landscape, intercellular crosstalk and tumor architecture of glioblastoma. Preprint at bioRxiv. https://doi.org/10.1101/2022.08.27.505439.

118. Kim, N., Kim, H.K., Lee, K., Hong, Y., Cho, J.H., Choi, J.W., Lee, J.-I., Suh, Y.-L., Ku, B.M., Eum, H.H., et al. (2020). Single-cell RNA sequencing demonstrates the molecular and cellular reprogramming of metastatic lung adenocarcinoma. Nat. Commun. *11*, 2285. https://doi.org/10.1038/s41467-020-16164-1.

119. Zhang, L., Zhang, Y., Wang, C., Yang, Y., Ni, Y., Wang, Z., Song, T., Yao, M., Liu, Z., Chao, N., et al. (2022). Integrated single-cell RNA sequencing analysis reveals distinct cellular and transcriptional modules associated with survival in lung cancer. Signal Transduct. Target. Ther. *7*, 9. https://doi.org/10.1038/s41392-021-00824-9.

120. Hirz, T., Mei, S., Sarkar, H., Kfoury, Y., Wu, S., Verhoeven, B.M., Subtelny, A.O., Zlatev, D.V., Wszolek, M.W., Salari, K., et al. (2023). Dissecting the immune suppressive human prostate tumor microenvironment via integrated single-cell and spatial transcriptomic analyses. Nat. Commun. *14*, 663. https://doi.org/10.1038/s41467-023-36325-2.

121. Zou, D.-D., Sun, Y.-Z., Li, X.-J., Wu, W.-J., Xu, D., He, Y.-T., Qi, J., Tu, Y., Tang, Y., Tu, Y.-H., et al. (2023). Single-cell sequencing highlights heterogeneity and malignant progression in actinic keratosis and cutaneous squamous cell carcinoma. eLife *12*, e85270. https://doi.org/10.7554/eLife.85270.

122. Kürten, C.H.L., Kulkarni, A., Cillo, A.R., Santos, P.M., Roble, A.K., Onkar, S., Reeder, C., Lang, S., Chen, X., Duvvuri, U., et al. (2021). Investigating immune and non-immune cell interactions in head and neck tumors by single-cell RNA sequencing. Nat. Commun. *12*, 7338. https://doi.org/10.1038/s41467-021-27619-4.

123. Werba, G., Weissinger, D., Kawaler, E.A., Zhao, E., Kalfakakou, D., Dhara, S., Wang, L., Lim, H.B., Oh, G., Jing, X., et al. (2023). Single-cell RNA sequencing reveals the effects of chemotherapy on human pancreatic adenocarcinoma and its tumor microenvironment. Nat. Commun. *14*, 797. https://doi.org/10.1038/s41467-023-36296-4.

124. Li, H., Zhou, J., Li, Z., Chen, S., Liao, X., Zhang, B., Zhang, R., Wang, Y., Sun, S., and Gao, X. (2023). A comprehensive benchmarking with practical guidelines for cellular deconvolution of spatial transcriptomics. Nat. Commun. *14*, 1548. https://doi.org/10.1038/s41467-023-37168-7.

125. Sang-aram, C., Browaeys, R., Seurinck, R., and Saeys, Y. (2024). Spotless, a reproducible pipeline for benchmarking cell type deconvolution in spatial transcriptomics. eLife *12*, RP88431. https://doi.org/10.7554/eLife.88431.

126. Chen, J., Liu, W., Luo, T., Yu, Z., Jiang, M., Wen, J., Gupta, G.P., Giusti, P., Zhu, H., Yang, Y., and Li, Y. (2022). A comprehensive comparison on cell-type composition inference for spatial transcriptomics data. Brief. Bioinform. *23*, bbac245. https://doi.org/10.1093/bib/bbac245.

127. Puram, S.V., Tirosh, I., Parikh, A.S., Patel, A.P., Yizhak, K., Gillespie, S., Rodman, C., Luo, C.L., Mroz, E.A., Emerick, K.S., et al. (2017). Single-Cell Transcriptomic Analysis of Primary and Metastatic Tumor Ecosystems in

Head and Neck Cancer. Cell *171*, 1611–1624.e24. https://doi.org/10.1016/j.cell.2017.10.044.

128. Dong, K., and Zhang, S. (2022). Deciphering spatial domains from spatially resolved transcriptomics with an adaptive graph attention auto-encoder. Nat. Commun. *13*, 1739. https://doi.org/10.1038/s41467-022-29439-6.

129. Wang, H., Li, J., Jing, S., Lin, P., Qiu, Y., Yan, X., Yuan, J., Tang, Z., Li, Y., Zhang, H., et al. (2025). SOAPy: a Python package to dissect spatial architecture, dynamics, and communication. Genome Biol. *26*, 80. https://doi.org/10.1186/s13059-025-03550-5.

130. Charrad, M., Ghazzali, N., Boiteau, V., and Niknafs, A. (2014). NbClust: An R Package for Determining the Relevant Number of Clusters in a Data Set. J. Stat. Softw. *61*, 1–36. https://doi.org/10.18637/jss.v061.i06.

131. Jin, S., Guerrero-Juarez, C.F., Zhang, L., Chang, I., Ramos, R., Kuan, C.-H., Myung, P., Plikus, M.V., and Nie, Q. (2021). Inference and analysis of cell-cell communication using CellChat. Nat. Commun. *12*, 1088. https://doi.org/10.1038/s41467-021-21246-9.

132. Hothorn, T., and Lausen, B. (2003). On the exact distribution of maximally selected rank statistics. Comput. Stat. Data Anal. *43*, 121–137. https://doi.org/10.1016/S0167-9473(02)00225-6.

133. Cable, D.M., Murray, E., Shanmugam, V., Zhang, S., Zou, L.S., Diao, M., Chen, H., Macosko, E.Z., Irizarry, R.A., and Chen, F. (2022). Cell type-specific inference of differential expression in spatial transcriptomics. Nat. Methods *19*, 1076–1087. https://doi.org/10.1038/s41592-022-01575-3.

134. Wu, T., Hu, E., Xu, S., Chen, M., Guo, P., Dai, Z., Feng, T., Zhou, L., Tang, W., Zhan, L., et al. (2021). clusterProfiler 4.0: A universal enrichment tool for interpreting omics data. Innovation *2*, 100141. https://doi.org/10.1016/j.xinn.2021.100141.

135. Smith, J.C., and Sheltzer, J.M. (2022). Genome-wide identification and analysis of prognostic features in human cancers. Cell Rep. *38*, 110569. https://doi.org/10.1016/j.celrep.2022.110569.

136. Tsoucas, D., Dong, R., Chen, H., Zhu, Q., Guo, G., and Yuan, G.-C. (2019). Accurate estimation of cell-type composition from gene expression data. Nat. Commun. *10*, 2975. https://doi.org/10.1038/s41467-019-10802-z.

137. Tran, K.A., Addala, V., Johnston, R.L., Lovell, D., Bradley, A., Koufariotis, L.T., Wood, S., Wu, S.Z., Roden, D., Al-Eryani, G., et al. (2023). Performance of tumour microenvironment deconvolution methods in breast cancer using single-cell simulated bulk mixtures. Nat. Commun. *14*, 5758. https://doi.org/10.1038/s41467-023-41385-5.

138. Dietrich, A., Merotto, L., Pelz, K., et al. (2026). omnideconv: a unifying framework for using and benchmarking single-cell-informed deconvolution of bulk RNA-seq data. Genome Biol. *27*, 6. https://doi.org/10.1186/s13059-026-03955-w.

139. Zhang, W., Zhang, X., Liu, Q., Wei, L., Qiao, X., Gao, R., Liu, Z., and Wang, X. (2025). Deconer: An Evaluation Toolkit for Reference-based Deconvolution Methods Using Gene Expression Data. Genom. Proteom. Bioinform. *23*, qzaf009. https://doi.org/10.1093/gpbjnl/qzaf009.

140. Adjusted Survival Curves. https://cran.r-project.org/web/packages/survival/vignettes/adjcurve.pdf.

141. Foster, K.. THE ARCSINE DIFFERENCE EFFECT MEASURE IN META-ANALYSIS WITH APPLICATION TO ADVERSE EVENTS FROM LONG-ACTING BETA-AGONISTS IN ASTHMA PATIENTS. https://etda.libraries.psu.edu/catalog/12357.

Please cite this article in press as: Li et al., Pan-cancer analysis of spatial transcriptomics reveals heterogeneous tumor spatial microenvironment, Cell Reports Medicine (2026), https://doi.org/10.1016/j.xcrm.2026.102751

CellPress
OPEN ACCESS

STAR★METHODS

KEY RESOURCES TABLE

REAGENT or RESOURCE	SOURCE	IDENTIFIER
Deposited data		
10× Visium datasets	Various public studies	See Table S1 for details
scRNA datasets	Various public studies	See Table S1 for details
Bulk RNA-Seq datasets	Various public studies	See Table S1 for details
Multiplexed protein imaging datasets	Various public studies	See Table S1 for details
MERSCOPE datasets	Vizgen official website	See Table S1 for details
Software and algorithms		
Seurat	https://satijalab.org/seurat/	version 4.3.0
spacexr	https://github.com/dmcable/spacexr	version 2.2.1
infercnv	https://github.com/broadinstitute/infercnv	version 1.10.1
scanpy	https://scanpy.readthedocs.io/en/latest/tutorials/index.html	version 1.10.3
STAGATE	https://stagate.readthedocs.io/en/latest/index.html	version 1.0.1
SOAPy	https://soapy-st.readthedocs.io/en/latest/Tutorials/index.html	version 1.0.1
entropy	https://cran.r-project.org/web/packages/entropy/index.html	version 1.3.1
NbClust	https://cran.r-project.org/web/packages/NbClust/index.html	version 3.0.1
ImmuneSubtypeClassifier	https://github.com/CRI-iAtlas/ImmuneSubtypeClassifier	version 0.1.0
clusterProfiler	https://bioconductor.org/packages/release/bioc/html/clusterProfiler.html	version 4.2.2
TCGAbiolinks	https://bioconductor.org/packages//release/bioc/html/TCGAbiolinks.html	version 2.23.1
survival	https://cran.r-project.org/web/packages/survival/index.html	version 3.5–5
maxstat	https://cran.r-project.org/web/packages/maxstat/	version 0.7–25
survminer	https://cran.r-project.org/web/packages/survminer/index.html	version 0.4.9
DWLS	https://github.com/dtsoucas/DWLS	version 0.1.0
meta	https://cran.r-project.org/web/packages/meta/	version 8.0–1
igraph	https://r.igraph.org/	version 1.5.0.1
tidygraph	https://cran.r-project.org/web/packages/tidygraph/index.html	version 1.2.3
ggraph	https://github.com/thomasp85/ggraph	version 2.1.0
ggplot2	https://cran.r-project.org/web/packages/ggplot2/index.html	version 3.5.1
ggupset	https://cran.r-project.org/web/packages/ggupset/index.html	version 0.4.0
ggalluvial	https://cran.r-project.org/web/packages/ggalluvial/index.html	version 0.12.5
ggvenn	https://cran.r-project.org/web/packages/ggvenn/index.html	version 0.1.10

(*Continued on next page*)

CellPress OPEN ACCESS

Cell Reports Medicine
Article

Continued

REAGENT or RESOURCE	SOURCE	IDENTIFIER
ggridges	https://cran.r-project.org/web/packages/ggridges/index.html	version 0.5.4
EnhancedVolcano	https://github.com/kevinblighe/EnhancedVolcano	version 1.12.0
aplot	https://github.com/YuLab-SMU/aplot	version 0.2.2
ggtree	https://github.com/YuLab-SMU/ggtree	version 3.2.1
patchwork	https://cran.r-project.org/web/packages/patchwork/index.html	version 1.2.0
ggforce	https://cran.r-project.org/web/packages/ggforce/index.html	version 0.4.1
ggrepel	https://cran.r-project.org/web/packages/ggrepel/index.html	version 0.9.3
ggh4x	https://cran.r-project.org/web/packages/ggh4x/index.html	version 0.2.8
jjPlot	https://github.com/junjunlab/jjPlot	version 0.0.2
circlize	https://cran.r-project.org/web/packages/circlize/index.html	version 0.4.15
ComplexHeatmap	https://github.com/jokergoo/ComplexHeatmap	version 2.10.0

METHOD DETAILS

Pan-cancer spatial transcriptomics data and preprocessing

10× Visium spatial transcriptomics (ST) data from 12 tumor types were collected from public databases and literatures, latest updated to January, 2024 (Table S1). The spot number, median UMI number, median feature number, median mitochondrial UMI percentage were summarized. Samples with 'spot number>500', 'median UMI>500' and 'median mitochondrial percentage<0.2' were reserved. After distinguishing the Benign/Stromal/Malignant compartments, we further filtered out the samples based on the following criteria: 1) the number of malignant spots is less than 100, or the number of malignant and stromal spots was less than 200; 2) the mean proportion of non-parenchymal cells in the malignant compartment was less than 0.7. Finally, total of 373 of all 421 samples were retained for analysis (Table S1). For downstream analysis, genes expressed in fewer than 3 spots were removed and mitochondrial genes were discarded for downstream analysis. These data preprocessing steps were carried out using Seurat (version 4.3.0).

Cell type deconvolution of 10× visium datasets

For each tumor type, we collected a representative scRNA-Seq dataset as a reference to perform cell type deconvolution for the ST data[43,113–123] (Tables S2 and S3). RCTD, one of the most recommended algorithms, was implemented in spacexr[62,124–126] (version 2.2.1) with the "full" mode. The deconvolution result was then normalized such that the sum of each spot was one.

Identification of tissue compartments

To partition each ST sample into distinct tissue compartments (Malignant, Stromal or Benign), we designed an automatic pipeline capable of accommodating the variability among samples and across different cancer types. For each 10× Visium sample, the proportions of non-parenchymal cells (including stromal and immune cells, *Pr*) in each spot were calculated. Since copy number alteration (CNA) primarily occurs in the genomes of malignant parenchymal cells, the top 1% of spots with the highest *Pr* values were used as reference spots, which were input into inferCNV (version 1.10.1) to identify CNA.[127] Few samples with too low *Pr* values (lowest *Pr* of the reference spots was higher than 0.5) were excluded, and all spots of these samples were labeled as "Malignant".

The spots were then clustered by gene expression similarity using the Lovain algorithm in Seurat package. CNV profiles acquired from run.final.infercnv were log transformed. After transformation, positive values indicate amplifications, while negative values indicate deletions. Spots within a cluster have similar expression profiles and cell compositions, thus we hypothesized that real CNV patterns would be highly consistent among spots within a cluster. Based on this hypothesis, the CNV values were further denoised as follows:

$$CNV'_{ij(c)} = \frac{CNV_{ij(c)}}{CV^{p}_{i(c)}}$$

Please cite this article in press as: Li et al., Pan-cancer analysis of spatial transcriptomics reveals heterogeneous tumor spatial microenvironment, Cell Reports Medicine (2026), https://doi.org/10.1016/j.xcrm.2026.102751

where $CNV_{ij(c)}$ and $CNV'_{ij(c)}$ are the CNV profiles of gene i in spot j belonging to cluster c before and after denoising, $CV_{ij(c)}$ is the coefficient of variation of gene i in spots belonging to cluster c:

$$CV_{i(c)} = \frac{\mathrm{std}(CNV_{i.(c)})}{\mathrm{mean}(CNV_{i.(c)})}$$

The lower bound of $CV_{ij(c)}$ is set to 0.5 to avoid extremely small values. p reflects the degree of denoising and $p = 0.5$ was selected to better retain real signal and removing noise.

Next, a *CNVscore* for a spot was defined as the sum of the squarse of all the genes' CNV values:

$$CNVscore_j = \sum_i CNV'^2_{ij}$$

and the *CNVscore* for a cluster $CNVscore_{(c)}$ was the mean CNV score of all spots within this cluster.

After that, the following strategy was used to classify spot clusters into Benign, Stromal or Malignant compartments.

1) The cluster with the maximum CNA score was defined as "Malignant_ref".
2) The clusters with higher *Pr* were recognized as "Stromal":

$$c = \text{Stromal, if } Pr(c) \geq Th$$

where the threshold (Th) of *Pr* was selected by Otsu's algorithm, which is a widely used binarization algorithm in image processing. Within the "Stromal" clusters, cluster with the lowest correlation with "Malignant_ref" was defined as "Stromal_ref".

3) For the remaining clusters, the mean CNV profiles of each cluster were adjusted by the proportion of non-parenchymal cells:

$$CNV'_{i(c)} \leftarrow CNV_{i(c)} \cdot \frac{1 - Pr_{(Malignant\_ref)}}{1 - Pr_{(c)}}$$

The clusters whose CNV profiles is more similar to "Malignant_ref" than that to "Stromal_ref" were classified as either "Malignant", or "Benign":

$$c_{c \neq Stromal} = \begin{cases} \text{Malignant } M < S \\ \text{Benign } M > S \end{cases}$$

where $M = \mathrm{dist}\left\{CNV'_{(c)}, CNV'_{(Malignant\_ref)}\right\}$, $S = \mathrm{dist}\left\{CNV'_{(c)}, CNV'_{(Stromal\_ref)}\right\}$, and "dist" is the Euclidean distance between the CNV profiles of two clusters.

Finally, the automatically assigned compartments were further validated through an examination of the spatial expression of known biomarkers specific to these compartments (Table S3). Since we focused on the TSME, spots of benign compartment among the samples were excluded from downstream analyses. Totally we identified 88,629 benign spots, 348,471 stromal spots and 556,280 malignant spots. Among all samples, 102 samples were identified as having benign compartments; 249 samples were identified as having only stromal and malignant compartments; 22 samples were identified as having only malignant compartment.

Characterization of LCPs in malignant and stromal compartments

Spots that have similar cell type compositions were defined as local cellular programs (LCPs). LCPs in the malignant and stromal compartments were identified separately. For the stromal compartment, only non-parenchymal cell types were considered and their proportions were normalized to make the sum one. For each type of tumor, top 1% of each cell type was clipped and then Z score normalized. Normalized values larger than three were clipped. The processed cell type composition matrix of all the spots was subsequently clustered with the k-means clustering algorithm implemented in R (iter.max = 100000, nstart = 40), and the number of clusters k was set 5 to 50. Finally, k = 32 and k = 29 was selected for MLCP and SLCP respectively, and finally 28 MLCPs and 28 SLCPs were obtained.

Connectivity score of the compartments

Neighboring spots were connected to construct a spatially adjacent network. We calculated the edges between compartments (N). We then shuffled the compartment labels of all the spots 20 times, and calculated the mean (m) and standard deviation (s) of the edges between the compartments under permutation. The Z score to reflect the connectivity between compartments compared with random distribution:

$$z - score(C_i, C_j) = \frac{N(C_i, C_j) - m(C_i, C_j)}{s(C_i, C_j)}$$

Unraveling the spatial distribution pattern of LCPs

As the malignant spots and stromal spots tend to aggregate with their own kind respectively, we defined the connectivity score between two kinds of LCP considering their compartment (Figures S3C and S3D). We built a spot interaction network according to their spatial location, in which spots located within two rounds were connected. We then computed the connectivity score to reflect the strength of the connection between LCPs. The connectivity score (CS) between LCP_i and LCP_j was defined differently considering their compartments:

$$CS(MLCP_i, MLCP_j) = \frac{N(MLCP_i, MLCP_j)}{N(MLCP., MLCP.)}$$

$$CS(MLCP_i, SLCP_j) = \frac{N(MLCP_i, SLCP_j)}{N(MLCP., SLCP.)}$$

$$CS(SLCP_i, SLCP_j) = \frac{N(SLCP_i, SLCP_j)}{N(SLCP., SLCP.)}$$

where $N(LCP_i, LCP_j)$ represents the number of edges between these two LCPs, and where *MLCP./SLCP.* represents all spots belonging to the malignant or stromal compartment. The *Z* score was calculated to compare the strength of connectivity with that under the random distribution:

$$z - score(LCP_i, LCP_j) = \frac{N(LCP_i, LCP_j) - \mu(LCP_i, LCP_j)}{s(LCP_i, LCP_j)}$$

where $\mu(LCP_i, LCP_j)$ and $s(LCP_i, LCP_j)$ are the mean and standard deviation of the number of the edges between these two LCPs under 20 times of permutations. The permutations were conducted by shuffling the LCP labels among the spots within each compartment. *CS* and *Z score* with LCP counts less than 10 would be expired for downstream analysis.

With these two indicators, we then describe the spatial distribution in the following two aspects.

1) *Z score*(LCP_i, LCP_j) was used to evaluate the self-connectivity of each LCP.
2) *CS*($MLCP_i$, $MLCP_j$) was used to identify the colocalization pattern of multiple niches. Mean CS across samples was calculated, and used to construct a weighted network reflecting LCP colocalization. In this network, edges with *Z* score not significantly less than zero (estimated by *t* test) were removed. We then used the Louvain community detection algorithm implemented in igraph (version 1.5.0.1) to identify communities under the resolution of 2.3.

Characterization of consensus niches

The spots located within two rounds nearest to the index spot were considered as its neighboring spots. The LCP composition of the neighboring spots was calculated, and the *Z* score was normalized within each tumor type. Normalized values larger than three were clipped. The processed neighboring LCP composition matrix was used for k-means clustering implemented in R (iter.max = 100000, nstart = 40), and the cluster number k was set 5–50. We selected the result from k = 42 and finally obtained 13 niches. Stable niche patterns were observed at different cluster number, and the LCPs colocalization. To compare our defined niches with the spatial domains based on gene expression, we applied STAGATE to identify spatial domains.[128]

Identifying niches using subcellular resolved spatial transcriptomics datasets

Publicly available MERSCOPE datasets were obtained from Vizgen's official website, comprising 13 FFPE samples analyzed with the 500-gene MERSCOPE Immuno-Oncology Panel across six cancer types (BRCA, CRC, HCC, NSCLC, OV, and PRAD). Quality control was performed where cells with fewer than 20 counts were filtered out. We performed PCA and batch effect correction across samples using bbknn (version 1.6.0), and subsequently applied Louvain clustering at a resolution of 1 to broadly categorize cells into tumor cells and tumor microenvironment (TME) cells. The TME cell subset was then extracted, underwent additional batch correction, and was reclustered at the resolution of 3, yielding distinct populations including fibroblasts, endothelial cells, CD4 T cells, CD8 T cells, NK, B cells, plasma cells, macrophages, cDCs, pDCs and mast cells. We then used our previously developed package SOAPy to identify niches.[129] We built a KNN network, which connects each cell with its nearest 30 cells. Then we calculated the cell type composition of its neighbors. Then the neighborhood cell type composition matrix was *Z* score normalized and the maximum value was limited to three. Based on that, we identified multi-cellular niches using k-means clustering.

Measurement of intra-tumor and inter-tumor heterogeneity

To measure intra-tumor heterogeneity, we used Shannon entropy to estimate the complexity of the niche composition within each sample:

Please cite this article in press as: Li et al., Pan-cancer analysis of spatial transcriptomics reveals heterogeneous tumor spatial microenvironment, Cell Reports Medicine (2026), https://doi.org/10.1016/j.xcrm.2026.102751

$$E = \sum_{i=1}^{N} p_i \cdot \log p_i$$

where p_i is the proportion of the i-th niche.

To elucidate inter-tumor heterogeneity, the niche compositions of all samples were used to conduct hierarchical clustering. We used Pearson's correlation coefficient and ward.D2 as the similarity metric and linkage criterion. Finally, we got 11 clusters, as indicated by the Dunn index, implemented in NbClust[130] (version 3.0.1). To compare sample clustering by niche types with previously defined pan-cancer immune subtypes,[64] we obtained sample-level expression matrix by summing up the UMIs from all spots in each ST sample, and then converting it to TPM matrix. The TPM matrix was input into ImmuneSubtypeClassfier[65] (https://github.com/CRI-iAtlas/ImmuneSubtypeClassifier) to assign the immune subtype for each ST sample.

Meta analysis by combining the rank of P-values

To combine the statistical results from each sample, we designed a method to evaluate the significance of the features comprehensively across samples. For each feature, the effect size (e.g., $\log_2$FC) and P-value from each sample were provided for meta analysis. First, the rank score of feature $g(1,2,\ldots,G)$ in sample $s(1,2,\ldots,S)$, denoted as R_{sg}, is defined as:

$$R_{sg} = \mathrm{rank}_{g=1}^{G}\left\{\mathrm{sign}\left(\mathrm{median}_{s=1}^{S} ES_{sg}\right) \cdot \left(-\mathrm{sign}\left(ES_{sg}\right) \cdot \log P_{sg}\right)\right\} \Big/ G$$

where ES_{sg} and P_{sg} represent the effect size and P-value of the hypothesis tests, respectively. The direction of the effect was determined by the sign of the median effect size of all samples, by which *-logP* of the features were ranked within each dataset in ascending or descending order decided.

After that, the ranks of each feature in all datasets were averaged, and the combined rank CR was defined as:

$$CR_g = \frac{\sum_{s=1}^{S} R_{sg}}{S}$$

The features with higher CRs have more significant positive or negative effectsd across samples. Singed CR is the product of the direction of the effect and CR, which displays the direction and significance of the effect simultaneously:

$$\text{Signed } CR_g = \mathrm{sign}\left(\mathrm{median}_{s=1}^{S}\ log\ ES_{sg}\right) \cdot CR_g$$

Finally, we calculated the number of total datasets, available datasets and datasets with significant effects. In addition, the available sample ratio (percentage of samples available for analysis) and significant study ratio (percentage of studies with significant effects in specific direction) were also provided.

This method has the following two advantages: 1) Compared with the methods that directly combining *p* values, it takes the direction of the effects of each single study into consideration, and is less sensitive to the outliers either; 2) The methods that employ fixed or random effect models have difficulty addressing those features missing in some datasets, which frequently occur in scRNA-Seq and ST data because of their sparsity. However, our method is effectiveunder these circumstances. This method is used for the analysis of LR interactions and NCDEGs which are mentioned below.

Niche-related LR interactions across samples

To decipher LR interactions within niches, the LR pairs collected from CellChatDB v1 were used for analysis.[131] For an LR pair consisting of *m* ligands and *n* receptors, their interaction score in a spot is defined as:

$$LR\ score = \sqrt{\left(\prod_{i=1}^{m} L_i\right)^{1/m} \cdot \left(\prod_{j=1}^{n} R_j\right)^{1/n}}$$

where L_i and R_j are the expressions of the i-th ligand and the j-th receptor in this spot respectively. For each sample, niche-related LR pairs were identified by comparing the LR scores of the spots across niches via FindAllMarkers. To acquire consensus LR pairs across samples, we used the meta analysis method mentioned above to summarize the inference result of each single sample, and LR pairs with 'available study ratio >1/3', 'significant study ratio >1/4' and 'signed CR > 0.5' were selected. We further dissected the LR pathways involved in each niche with enrichment analysis. The pathways with less than five LR pairs were removed. Fisher's exact test was used and $p < 0.05$ are recognized as LR pairs enriched in specific interaction pathways in the niches.

To further explore the clinical relevance of LRs, we obtained the bulk RNA-seq data and survival data from the TCGA project. The geometric mean of the ligand and receptor was calculated to quantify the interaction strength of the LR in each sample. The optimal cutoff was determined using maxstat[132] (version 0.7–25), based on which the hazard ratio and P-value were calculated with Cox proportional hazard regression to compare the effects on the prognosis of patients between two groups.

CellPress OPEN ACCESS

Cell Reports Medicine
Article

Determination of the NCDEGs

We applied C-SIDE implemented by spacexr, a software for inference of cell type-specific differential expression based on the result of cell type composition from RCTD.[133] C-SIDE was performed for each single sample with the parameters cell_type_threshold = 30 and gene_threshold = 5e−05. Before that, we removed the samples where the number of spots in any niches for comparison was less than 50. For the NCDEGs of tumor cells, we compared Niche_2 – Niche_6 with Niche_1, the latter of which was considered as the spots only with parenchymal cell. For the NCDEGs of macrophages, we conducted C-SIDE to identify macrophage-specific differential expressed genes between Niche_11 and Niche_4, as well as between Niche_11 and Niche_10. Our meta analysis method was applied again to combine the results from single samples. We adopted the genes existing in the results of more than 1/3 of the samples for meta analysis. We kept the genes with 'significant study ratio' greater than 0.3 for tumor cell and 0.25 for macrophage, as well as 'signed CR' larger than 0.5 or less than −0.5. Furthermore, NCDEG of tumor cell in different niches by enrichment analysis implemented by clusterProfiler[134] (version 4.2.2). *p* value was adjusted by Benjamini-Hochberg method and adjusted *p* value less than 0.05 was selected.

To visualize the NCDEG within sample, we constructed a "Gene expression – Cell type fraction" scatterplot, which was grouped by niches. Furthermore, we built a linear model:

$$Exp = \beta_0 + \beta_1 \cdot ct + \beta_2 \cdot niche + \beta_3 \cdot (ct \cdot niche)$$

where *ct* represents the fraction of the cell type and *niche* is a binary variable representing whether the spot belongs to specific niche. In this model, β_2 and β_3 reflect the effects of the NCDEG.

Clinical implications of niches using bulk RNA-Seq datasets

For TCGA datasets, the TPM expression matrices and molecular subtypes were downloaded via TCGAbiolinks, and the clinical data was obtained.[135] For immunotherapy datasets, we downloaded the expression matrix and response to therapy. The TPM expression matrixes and corresponding scRNA-Seq references were input into DWLS (version 0.1.0) to infer the cell type composition for bulk RNA-Seq.[136–139] Within each tumor type or treatment cohort, the proportion of each cell type was *Z* score normalized. Then, based on whether the normalized values were positive or negative, the data were further binarized to determine if the cell type existed in each sample. The niche type of each bulk sample was assigned according to the presence of cell types.

The TCGA datasets were used to analyze the associations between niches and overall survival time. First, we evaluated their effects in pan-cancer data using the Cox proportional hazard regression model implemented in the survival package (version 3.5–5), with niche type and tumor type set as variables. The adjusted survival curves with tumor type as covariates, were generated using ggadjustedCurves (method = "marginal") implemented in the survminer package (version 0.4.9).[140] In addition, we compared the effect of survival between any two niches using the Cox proportional hazard regression model with tumor type as covariates. For each type of tumor, we used the log rank test to compare the survival differences among patients with different niche types.

To clarify the associations between the niches and the response to immunotherapy, we utilized datasets of eight cohorts containing 776 patients (four NSCLC and two KIRC datasets for patients treated with immunotherapy; one NSCLC dataset for patients treated with immunotherapy and chemotherapy; and one PRAD dataset for patients treated with immunotherapy and anti-androgen receptor therapy) and conducted meta analysis with metabin implemented in meta (version 8.0-1). We applied the arcsine transformed-rate difference (ASD) as statistic, suitable for cohorts with low sample size,[141] before which we use the Q-statistic to examine the between-study heterogeneity and determine the common or random effect model.

Clinical implications of the spatial distribution of macrophages using multiplexed protein imaging data

To validate the clinical implications of macrophage-related niches, we collected four datasets from multiplexed protein imaging, three of which were used to evaluate the survival effect, and the remaining one was used to evaluate the response to immunotherapy. For each macrophage, we compared its distance to the nearest tumor cell and T cell, after which the macrophages were classified into two categories: M01 denoted macrophages proximal to T cells, whereas M02 referred to those proximal to the tumor cells. The patients were stratified into four groups by the median proportion of M01 and M02: patients of G1 contains high proportion of M01 and low proportion of M02; patients of G2 contains high proportion of both M01 and M02; patients of G3 contains low proportion of both M01 and M02; patients of G4 contains high proportion of M02 and low proportion of M01. We compared the survival time among four patient groups by log rank test, and compared their response to immunotherapy by Fisher's exact test.

QUANTIFICATION AND STATISTICAL ANALYSIS

The details of the statistical tests were shown in figure legends and STAR Methods. Boxplots display the lower quartile, the median (center line), the upper quartile.